The Journal of Chemical Physics

Intermolecular vibrational states of HF trimer from rigorous nine-dimensional quantum calculations: Strong coupling between intermolecular bending and stretching vibrations and the importance of the three-body interactions

Cite as: J. Chem. Phys. **157**, 194103 (2022); https://doi.org/10.1063/5.0128550
Submitted: 28 September 2022 • Accepted: 27 October 2022 • Accepted Manuscript Online: 27 October 2022 • Published Online: 15 November 2022

Peter M. Felker and Zlatko Bačić

AIP Publishing

The Journal of Chemical Physics ARTICLE scitation.org/journal/jcp

Intermolecular vibrational states of HF trimer from rigorous nine-dimensional quantum calculations: Strong coupling between intermolecular bending and stretching vibrations and the importance of the three-body interactions

Cite as: J. Chem. Phys. 157, 194103 (2022); doi: 10.1063/5.0128550
Submitted: 28 September 2022 • Accepted: 27 October 2022 •
Published Online: 15 November 2022

Peter M. Felker[1,a] and Zlatko Bačić[2,3,4,a]

AFFILIATIONS

[1] Department of Chemistry and Biochemistry, University of California, Los Angeles, California 90095-1569, USA
[2] Department of Chemistry, New York University, New York, New York 10003, USA
[3] Simons Center for Computational Physical Chemistry at New York University, New York, New York 10012, USA
[4] NYU-ECNU Center for Computational Chemistry at NYU Shanghai, 3663 Zhongshan Road North, Shanghai 200062, China

[a] **Authors to whom correspondence should be addressed:** felker@chem.ucla.edu and zlatko.bacic@nyu.edu

ABSTRACT

We present the computational methodology that allows rigorous and efficient nine-dimensional (9D) quantum calculations of the intermolecular vibrational states of noncovalently bound trimers of diatomic molecules, with the monomers treated as rigid. The full 9D vibrational Hamiltonian of the trimer is partitioned into a 3D "frame" (or stretching) Hamiltonian and a 6D "bend" Hamiltonian. These two Hamiltonians are diagonalized separately, and a certain number of their lowest-energy eigenstates is included in the final 9D product contracted basis in which the full 9D intermolecular vibrational Hamiltonian is diagonalized. This methodology is applied to the 9D calculations of the intermolecular vibrational levels of $(HF)_3$, a prototypical hydrogen-bonded trimer, on the rigid-monomer version of an *ab initio* calculated potential energy surface (PES). They are the first to include fully the stretch-bend coupling present in the trimer. The frequencies of all bending fundamentals considered from the present 9D calculations are about 10% lower than those from the earlier quantum 6D calculations that considered only the bending modes of the HF trimer. This means that the stretch-bend coupling is strong, and it is imperative to include it in any accurate treatment of the $(HF)_3$ vibrations aiming to assess the accuracy of the PES employed. Moreover, the 9D results are in better agreement with the limited available spectroscopic data that those from the 6D calculations. In addition, the 9D results show sensitivity to the value of the HF bond length, equilibrium or vibrationally averaged, used in the calculations. The implication is that full-dimensional 12D quantum calculations will be required to obtain definitive vibrational excitation energies for a given PES. Our study also demonstrates that the nonadditive three-body interactions are very significant in $(HF)_3$ and have to be included in order to obtain accurate intermolecular vibrational energy levels of the trimer.

I. INTRODUCTION

Molecular complexes bound by noncovalent, hydrogen-bonded and van der Waals, interactions have been the subject of intense research activity by experimentalists and theorists alike for decades, and the attention they receive continues unabated. So far, these investigations have focused overwhelmingly on the weakly bound molecular dimers. The quantum calculations of their (ro)vibrational states and spectra have generally been performed under the assumption of rigid monomers, motivated by the large disparity, typically an order of magnitude or more, between the frequencies of the intramolecular vibrations of the monomers and the

intermolecular vibrations of the complexes.[1–4] A significant step forward was made by the full-dimensional quantum calculations of $(HF)_2$, $(DF)_2$, and HFDF,[5] as well as $(HCl)_2$,[6,7] for the monomers in their ground vibrational states. However, certain widely measured spectroscopic properties of molecular dimers, such as the intramolecular vibrational frequencies and their shifts from the gas-phase monomer values, as well as the changes in tunneling splittings upon intramolecular vibrational excitations, can be reliably obtained only from fully coupled quantum calculations in full dimensionality that extend to excited vibrational states of flexible monomers. Until recently, only a few such comprehensive, computationally highly demanding treatments were reported for $(HF)_2$[8–11] and $(HCl)_2$.[12] Intra- and intermolecular (ro)vibrational states of $(H_2O)_2$ were the subject of the [6 + 6]D adiabatic approach[13–15] and fully coupled quantum twelve-dimensional (12D) calculations that reached the manifold of the excited water bend vibrations.[16] Methodological advances made by us in the past couple of years[11] have enabled full-dimensional and fully coupled quantum treatments of several noncovalently bound triatom–diatom complexes—H_2O/D_2O–CO,[17] HDO–CO,[18] H_2O–HCl,[19] and several H/D isotopologues,[20,21] the first to yield converged energies of all intramolecular vibrational fundamentals, together with low-lying intermolecular vibrational states, for molecular dimers with more than four atoms.

Clearly, in the case of the noncovalently bound molecular dimers, the methodologies for full-dimensional and fully coupled quantum calculation of their intra- and intermolecular (ro)vibrational eigenstates have reached a high degree of sophistication and power. Through comparison between the rigorously calculated rovibrational eigenstates and spectra of the dimers with the corresponding experimental far-infrared (FIR), mid-IR, and Raman spectroscopic data, it is now possible to reliably assign the latter and also test the quality of the potential energy surfaces (PESs) employed and guide their refinement. Moreover, the dimer PESs determined in this way can be used to construct the two-body interaction potentials, the dominant component of the many-body representation of the PESs for aggregates of noncovalently bound molecules. For example, in the case of $(HCl)_n$ clusters,[22] the two-body potential was obtained from the 6D ES1-EL PES of the HCl dimer,[12] which accurately predicts many spectroscopic properties of this dimer. The evident impressive progress in the rigorous quantum calculations of the rovibrational states of the noncovalently bound molecular dimers provides a strong motivation for its extension to weakly bound molecular trimers and, eventually, larger molecular clusters.

Noncovalently bound molecular trimers hold a special place in the hierarchy of molecular clusters. These are the smallest clusters in which the nonadditive many-body (three-body in this case) interactions arise, terms that are essential for accurate description of the structural and dynamical properties of condensed phases. Consequently, molecular trimers are the obvious, most natural candidates for sensitive testing of the computed three-body interactions through comparison of high-level bound state calculations with the spectroscopic datasets. However, this presupposes the existence of such a rigorous quantum methodology for weakly bound molecular trimers, which is not the case at the present time.

An obvious obstacle to its development is the high dimensionality of the trimers. Thus, for $(H_2O)_3$, the full intra- and intermolecular vibrational problem is 21D. Its dimensionality is reduced to 12D if the monomers are treated as rigid, which is likely to be manageable eventually, but only after major, time-consuming methodological and computational efforts. In the meantime, the vibrational states of $(H_2O)_3$ and its isotopologues have been calculated by a variety of approximate treatments. Some of them involved variational calculations in the reduced-dimension subspaces of either the torsional, or flipping, motions of the three free O–H bonds around each of the hydrogen-bonded O–H bonds,[23–30] or the intramolecular vibrations of the three water moieties.[31] The vibrational levels of $(H_2O)_3$ were calculated in the vibrational self-consistent field (VSCF)[32] and harmonic[33] approximations. Finally, the tunneling splittings in the ground state of $(H_2O)_3$ were calculated by means of the fixed-node diffusion Monte Carlo (DMC) method[33,34] and also using the ring-polymer instanton approach.[35–37]

Noncovalently bound molecular trimers comprised of diatomic moieties, e.g., $(HF)_3$ and $(HCl)_3$, in principle, offer better and more immediate prospects for rigorous quantum calculations of their vibrational levels, owing to their lower dimensionality, 12D for flexible monomers and 9D if the monomers are taken to be rigid. Yet, the only molecular trimer to date for which fully coupled quantum bound-state calculations has been reported is $(H_2)_3$ for rigid monomers[38] and in full dimensionality,[39] in both cases finding only one bound state for each symmetry. The very weakly bound $(H_2)_3$ is a special case, and the methodologies used in these two calculations have not been applied to any other more strongly bound molecular trimer.

Motivated by the present unsatisfactory situation, in this paper, we introduce the computational methodology for rigorous 9D quantum calculations of the intermolecular vibrational states of noncovalently bound trimers of diatomic molecules. The only dynamical approximation made in this treatment is keeping the bond lengths of the three monomers fixed. This assumption is certainly reasonable for $(HF)_3$, given that the intramolecular HF stretch frequencies (close to 4000 cm^{-1}) are considerably higher than those of the intermolecular bends (under 1000 cm^{-1}) and intermonomer stretches (under 200 cm^{-1}). The approach is designed with more strongly bound molecular trimers in mind, such as the hydrogen-bonded HF and HCl trimers with many intermolecular vibrational states and where three-body interactions are expected to play an important role. We chose $(HF)_3$, a paradigmatic hydrogen-bonded trimer, for the initial implementation of the new methodology because of the availability of a full-dimensional PES, as well as some pertinent spectroscopic data in the literature. In addition, several lower-dimensional quantum bound-state calculations have been published previously, which offer at least a partial comparison with the 9D results reported here.

A comprehensive review of the early spectroscopic and quantum dynamics studies of HF clusters, including the trimer, is available.[40] These studies are also covered in Ref. 1. From the IR spectra of $(DF)_3$[41] and the FIR spectra of $(HF)_3$,[42] both in supersonic jets, it was determined that the two isotopologues have a cyclic structure that, owing to the vibrational averaging, is that of an oblate symmetric top. The measured gas-phase frequencies of the degenerate intramolecular HF and DF stretch fundamentals of the trimers are 3712[43,44] and 2724.6 cm^{-1},[41] respectively. Experimental information about the intermolecular vibrations of the HF and DF trimers

is limited. For $(HF)_3$, some of it comes from the spectroscopy in Ne[45] and Ar[46] matrices. In addition, two bands, at 494 and 602 cm^{-1}, appear in the FIR spectrum of the gas-phase $(HF)_3$,[42] and are attributed to the in-plane and out-of plane bending fundamentals, respectively.

On the theory side, Quack, Stohner, and Suhm have constructed several PESs for $(HF)_3$ and larger HF aggregates,[47,48] all of them represented as a sum of many-body terms. They combined two different analytical 12D three-body terms obtained from *ab initio* electronic structure calculations with the two-body terms extracted from the *ab initio* calculated and empirically refined PESs for HF dimer.[49,50] Quack *et al.* used these PESs and the DMC method to calculate the binding energies D_0 and other dynamical properties of HF oligomers, but not their intermolecular vibrational eigenstates.[47,48] In addition, Io *et al.*[51] have performed *ab initio* path integral molecular dynamics simulations of $(HF)_3$ in order to investigate the role of the nuclear quantum effects in stabilizing the hydrogen-bonding network in the trimer. Anharmonic intra- and intermolecular vibrational frequencies of $(HF)_3$ have been calculated utilizing the vibrational self-consistent field (VSCF) method[52] and also by obtaining the harmonic frequencies at the high level of *ab initio* electronic structure theory and then computing their anharmonic corrections at the MP2 level.[42]

Variational calculations of the intermolecular vibrational levels of $(HF)_3$ have so far been limited to the bending (or torsional) levels only, with the three intermonomer center-of-mass (c.m.) distances and HF bond lengths held fixed. In the first such study by Kolebrander *et al.*,[44] the three in-plane bends were treated separately, as decoupled from the three out-of plane bends, leading to two separate 3D quantum calculations. Subsequently, Wang and Carrington went one step further and performed 6D quantum calculations of the bending levels of $(HF)_3$ and $(DF)_3$,[53] where the in-plane and out-of-plane bends were treated as coupled, and all other degrees of freedom (DOFs), intra- and intermolecular, as frozen. As a result, both studies left unanswered the key question of the coupling between the intermolecular bending and stretching DOFs of the trimer, and its effects on the intermolecular vibrational states. This coupling is expected to be significant in $(HF)_3$ (and the results presented here confirm this). In the absence of such information, and the uncertainty that it creates, the computed bending levels cannot be used with confidence to assess the quality of the PESs employed, nor to assign reliably the bands in the measured spectra.

The quantum 9D calculations reported in this paper are the first to include all intermolecular DOFs of $(HF)_3$ in a rigorous manner. Consequently, they can, and do, characterize accurately the strength of the stretch-bend coupling in this prototypical hydrogen-bonded trimer, and its manifestations in the intermolecular vibrational level structure. A three-body PES by Quack *et al.*[48] is employed in the present calculations. It combines the SO-3 two-body potential[50] with the three-body term designated HF3BG.[48] Hereafter, this $(HF)_3$ PES is referred to as SO-3 + HF3BG. The same PES was used by Wang and Carrington in their quantum 6D calculations of the bending energy eigenstates of $(HF)_3$.[53] Consequently, direct comparison can be made between their 6D results and the present ones in 9D. Significant difference between the two sets of results is found, demonstrating that the stretch-bend coupling is strong in $(HF)_3$. Therefore, reduced-dimension bound-state calculations that do not include the stretch-bend coupling, such as those in 6D of the bending states alone, cannot provide a reliable assessment of the accuracy of the PES employed. A comparison is also made with the available experimental data in the literature, which is unfortunately scant. It shows that including the stretch-bend coupling in the 9D calculations improves significantly the agreement between theory and experiment, over that for the 6D calculations.

This paper is organized as follows: Computational methodology is described in Sec. II. In Sec. III, we present and discuss the results. Section IV contains the conclusions.

II. COMPUTATIONAL METHODOLOGY

A. Coordinates and Hamiltonian

We follow Wang and Carrington[54] in using the following coordinates, depicted schematically in Fig. 1, for the cyclic $(HF)_3$ in the rigid-monomer approximation:

(1) The intermolecular "frame" coordinates: The three monomer-c.m.-to-monomer-c.m. distances, R_k (k = 1–3), where R_1 is the distance from monomer 2 to monomer 3, R_2 that from monomer 1 to monomer 3, and R_3 that from monomer 1 to monomer 2. They are equivalent to the intermolecular stretching coordinates, and in the later sections of this paper, the vibrations primarily associated with them will be referred to as the intermolecular stretching vibrations.

(2) The intermolecular "bend" coordinates: The six local polar and azimuthal angles (θ_k, ϕ_k), (k = 1–3) that fix the orientation of the monomer-k internuclear vector $\mathbf{r}_k$ (which points from the F nucleus to the H nucleus of monomer k) with respect to a local Cartesian axis system centered at the c.m.

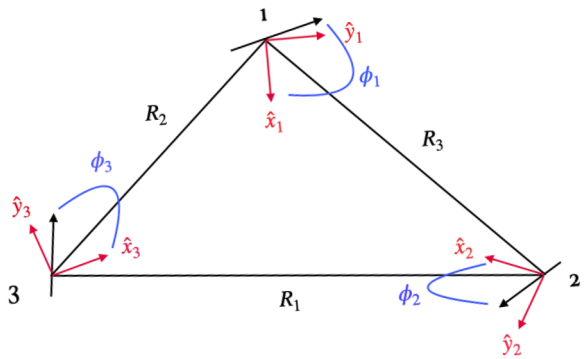

FIG. 1. Schematic depiction of the coordinates used for the cyclic HF timer. Shown explicitly are the six in-plane coordinates: the three monomer-c.m.-to-monomer-c.m. distances R_k (k = 1–3), and the three azimuthal angles ϕ_k (k = 1–3). Also shown are the (in-plane) $\hat{x}_k$ and $\hat{y}_k$ axes of local Cartesian systems centered at the c.m. of monomer k (k = 1–3). The (out-of-plane) $\hat{z}_k$ (k = 1–3) axes (not shown) are parallel to the vector $\mathbf{R}_1 \times \mathbf{R}_2$, i.e., perpendicular to the plane defined by the c.m.s of the three monomers. For each monomer k the polar angle θ_k is the angle between the HF internuclear vector $\mathbf{r}_k$ and the local $\hat{z}_k$ axis. Together, θ_k and ϕ_k define the orientation of $\mathbf{r}_k$ (k = 1–3) relative to the local Cartesian axis system attached to monomer k. In the equilibrium geometry on the SO-3 + HF3BG PES, for $\bar{r} = r_e$, $R_1 = R_2 = R_3$ = 4.760 07 bohrs, θ_k = 90° (k = 1–3), and ϕ_k = 54.019 79° (k = 1–3). For additional details, see the text.

of monomer k. In each of the local axis systems, the $\hat{z}_k$ axis is parallel to the vector $\mathbf{R}_1 \times \mathbf{R}_2$, where $\mathbf{R}_1$ is the vector from the c.m. of monomer No. 3 to that of monomer No. 2 and $\mathbf{R}_2$ is the vector from the c.m. of monomer No. 3 to that of monomer No. 1. The $\hat{x}_k$ axis is parallel to the bisector of the interior angle (α_k) of the triangle formed by the three monomer c.m.s with vertex at the kth c.m, and $\hat{y}_k = \hat{z}_k \times \hat{x}_k$. Finally, $\cos\theta_k \equiv \mathbf{r}_k \cdot \hat{z}_k/|\mathbf{r}_k|$ and $\tan\phi_k = \mathbf{r}_k \cdot \hat{y}_k/\mathbf{r}_k \cdot \hat{x}_k$.

With these coordinates [we henceforth denote all of the R_k collectively as R and all of the (θ_k, ϕ_k) coordinates collectively as ω] and for a Wilson-type[55] volume element given by $d\sigma = \Pi_{k=1}^{3}(dR_k \sin\theta_k d\theta_k d\phi_k)$, the $J = 0$ rigid-monomer vibrational Hamiltonian can be written as[54]

$$\hat{H} = \hat{K}_{M,rot} + \hat{K}_M + \hat{K}_F + \hat{V}' + \hat{K}_{FM} + V. \tag{1}$$

Here, $\hat{K}_{M,rot}$ is the rotational kinetic energy operator for all three monomers

$$\hat{K}_{M,rot}(\omega) \equiv \sum_{k=1}^{3} B_M \hat{l}_k^2, \tag{2}$$

with $\hat{l}_k^2$ the operator corresponding to the square of the rotational angular momentum of monomer k and B_M the HF-monomer rotational constant. $\hat{K}_M = \hat{K}_M^{(1)} + \hat{K}_M^{(2)}$ is an operator corresponding to the contribution to the kinetic energy from the angular momenta of the monomers projected onto the trimer frame,

$$\hat{K}_M^{(1)}(R,\omega) \equiv \sum_{k=1}^{3} \frac{1}{2}\Big[M_{xx}^{(k)}\hat{l}_{kx}^2 + M_{yy}^{(k)}\hat{l}_{ky}^2 + M_{zz}^{(k)}\hat{l}_{kz}^2 + M_{xy}^{(k)}(\hat{l}_{kx}\hat{l}_{ky} + \hat{l}_{ky}\hat{l}_{kx})\Big] \tag{3}$$

and

$$\hat{K}_M^{(2)}(R,\omega) \equiv \sum_{k<i}^{3}\Big[M_{xx}^{(ki)}\hat{l}_{kx}\hat{l}_{ix} + M_{yy}^{(ki)}\hat{l}_{ky}\hat{l}_{iy} + M_{zz}^{(ki)}\hat{l}_{kz}\hat{l}_{iz} + M_{xy}^{(ki)}\hat{l}_{kx}\hat{l}_{iy} + M_{yx}^{(ki)}\hat{l}_{ky}\hat{l}_{ix}\Big], \tag{4}$$

where $\hat{l}_{k\alpha}$ $(\alpha = x, y, z)$ is the operator corresponding to the projection of the angular momentum of monomer k onto the αth local trimer-fixed axis, and the $M_{qq'}^{(k)}$ and $M_{qq'}^{(ki)}$ are coefficients depending only on the R_k and the monomer masses (M_k) [see Eqs. (25) and (27) of Ref. 54] $\hat{K}_F$ is the kinetic energy of the three-c.m. frame,

$$\hat{K}_F(R) \equiv \sum_{k=1}^{3}\left[-\frac{1}{2\mu_k}\frac{\partial^2}{\partial R_k^2} - \frac{\cos\alpha_k}{R_1R_2R_3}\left(\frac{R_l^2}{M_l} + \frac{R_m^2}{M_m}\right)\frac{\partial}{\partial R_k}\right] - \left[\frac{\cos\alpha_1}{M_1}\frac{\partial^2}{\partial R_2\partial R_3} + \frac{\cos\alpha_1}{M_1}\frac{\partial^2}{\partial R_2\partial R_3} + \frac{\cos\alpha_3}{M_3}\frac{\partial^2}{\partial R_1\partial R_2}\right]. \tag{5}$$

$\hat{V}'$ is a potential-like term in the kinetic energy

$$\hat{V}'(R) \equiv \frac{\frac{R_1^4}{M_1^2} + \frac{R_2^4}{M_2^2} + \frac{R_3^4}{M_3^2}}{8R_1^2R_2^2R_3^2}. \tag{6}$$

[We note that Eq. (6) differs from Eq. (33) of Ref. 54. The latter has a misprint that omits the monomer mass factors.] $\hat{K}_{FM}$ is a frame-monomer coupling contribution to the kinetic energy,

$$\hat{K}_{FM}(R,\omega) \equiv i\sum_{k=1}^{3}\left(\lambda_z^{(k)} + \frac{1}{2}h_z^{(k)}\right)\hat{l}_{kz} \tag{7}$$

with

$$\lambda_z^{(k)} \equiv \frac{1}{2}\left[\frac{\sin\alpha_k}{M_k}\left(\frac{1}{R_l}\frac{\partial}{\partial R_m} - \frac{1}{R_m}\frac{\partial}{\partial R_l}\right) + \left(\frac{\sin\alpha_l}{M_lR_m} - \frac{\sin\alpha_m}{M_mR_l}\right)\frac{\partial}{\partial R_k}\right], \tag{8}$$

$$h_z^{(k)} \equiv \frac{\cot\alpha_k}{2}\left(\frac{1}{\mu_mR_m^2} - \frac{1}{\mu_lR_l^2}\right) + \frac{1}{2R_k}\left(\frac{\sin\alpha_m}{M_mR_l} - \frac{\sin\alpha_l}{M_lR_m}\right), \tag{9}$$

and (k, l, m) a cyclic permutation of (1, 2, 3).

Finally, $V(R,\omega)$ is the 9D intermolecular potential-energy function. We take V to be the rigid-monomer version of the SO-3 + HF3BG surface computed by Quack, Stohner, and Suhm,[47] which includes one-, two-, and three-body terms. Note that both V and $\hat{K}_{M,rot}$ depend on the choice of the fixed rigid-monomer bond distance, which we label $\bar{r}$. In this work, we present results for two different values of $\bar{r}$. One of them, $r_e = 1.763\,794\,8$ bohrs, is the monomer equilibrium bond distance on the SO-3 + HF3BG surface.[53] The other is $r_0 = 1.781\,311\,4$ bohrs, a very good estimate of the ground-state expectation value of the monomer internuclear distance on that surface. As outlined in Sec. III C, it was obtained from the quantum 3D calculation of the intramolecular vibrational states of $(HF)_3$ for the intermolecular coordinates frozen at their expectation values associated with the intermolecular (3D) frame and (6D) bending ground states, respectively.

B. General approach

Our contracted-basis approach to solving for the eigenstates of $\hat{H}$ is similar to that employed by Wang and Carrington in their 9D study of the vibrational states of methane.[56] We diagonalize $\hat{H}$ in three steps. In the first two, we diagonalize the reduced "frame" and "bend" Hamiltonians, $\hat{H}_F$ and $\hat{H}_B$, respectively.

The 3D $\hat{H}_F$ for a given $\bar{r}$ is defined as

$$\hat{H}_F(R;\bar{\omega},\bar{r}) \equiv \hat{K}_F(R) + V'(R) + V_F(R;\bar{\omega},\bar{r}), \tag{10}$$

where $V_F(R;\bar{\omega},\bar{r})$ is a 3D frame potential-energy function derived from V and *symmetrized* so as to be invariant under the operations of the G_{12} molecular symmetry group[53] characterizing $(HF)_3$. Here, $\bar{\omega}$ represents the means by which the ω angle variables in V are fixed so as to extract V_F from the 9D V. (We have tested two different ways of doing this, which we describe in Sec. II C 1.) With such a choice for V_F, it is easy to see that $\hat{H}_F$ is invariant under the operations of G_{12}. We denote the N_F lowest-energy eigenvectors and eigenvalues of $\hat{H}_F$, respectively, as $|\rho\rangle$ and $E_\rho^{(F)}$ $(\rho = 1, 2, \ldots, N_F)$.

The 6D $\hat{H}_B$ is defined as

$$\hat{H}_B(\omega;\bar{R},\bar{r}) \equiv \hat{K}_{M,rot}(\omega;\bar{r}) + \hat{K}_M(\omega;\bar{R}) + V_B(\omega;\bar{R},\bar{r}), \tag{11}$$

where $\bar{R}$ represents a fixed value for of all of the intermonomer distances R_k and V_B is the 6D PES obtained by evaluating V at the fixed intermonomer distances $R_k = \bar{R}$ and the fixed intramonomer

distances $r_k = \bar{r}$. By using the explicit expressions[54] for $\hat{K}_{M,rot}(\omega;\bar{r})$ and $\hat{K}_M(\omega;\bar{R})$, one can show that

$$\hat{H}_B(\omega;\bar{R},\bar{r}) = \sum_{k=1}^{3}\left[(B_M+B_F)\hat{l}_k^2 - \frac{3}{8}B_F\hat{l}_{kz}^2\right] + B_F\sum_{k<n}^{3}\left[-(\hat{l}_{kx}\hat{l}_{nx}+\hat{l}_{ky}\hat{l}_{ny}) + \frac{7}{8}\hat{l}_{kz}\hat{l}_{nz} + \sqrt{3}(\hat{l}_{kx}\hat{l}_{ny}-\hat{l}_{ky}\hat{l}_{nx})\right] + V_B(\omega;\bar{R},\bar{r}), \quad (12)$$

where $B_M \equiv (2\mu_r\bar{r}^2)^{-1}$, $B_F \equiv (M\bar{R}^2)^{-1}$, μ_r is the reduced mass of each monomer, and $M = M_k$ $(k = 1\text{–}3)$ is the mass of each monomer. Note that $\hat{H}_B$ is invariant under the operations of G_{12}. [Note also that the KEO (kinetic energy operator) of our $\hat{H}_B$ is slightly different than the properly "constrained" bend KEO for the trimer—see Eq. (23) of Ref. 53.] We denote the N_B lowest-energy eigenvectors and corresponding eigenvalues of $\hat{H}_B$, respectively, as $|\kappa\rangle$ and $E_\kappa^{(B)}$ $(\kappa = 1,2,\ldots,N_B)$.

In the final step, we diagonalize the full 9D Hamiltonian, which can now be re-written as

$$\hat{H} = \hat{H}_F + \hat{H}_B + \hat{K}_{FM} + \Delta\hat{K}_M + \Delta V, \quad (13)$$

where

$$\Delta\hat{K}_M(\omega,R;\bar{R}) \equiv \hat{K}_M(\omega,R) - \hat{K}_M(\omega;\bar{R}) \quad (14)$$

and

$$\Delta V(R,\omega;\bar{\omega},\bar{R},\bar{r}) \equiv V(R,\omega;\bar{r}) - V_F(R;\bar{\omega},\bar{r}) - V_B(\omega;\bar{R},\bar{r}). \quad (15)$$

We do this by using a contracted product basis of the form

$$|\rho,\kappa\rangle \equiv |\rho\rangle|\kappa\rangle, \quad (16)$$

with the contraction affected by keeping only those states with $E_\rho^{(F)}$ and $E_\kappa^{(B)}$ below cut-off values. In such a basis, the matrix elements of the $\hat{H}_F + \hat{H}_B$ portion of $\hat{H}$ are diagonal and trivially obtained. Calculation of the matrix elements of $\hat{K}_{FM}$, $\Delta\hat{K}_M$, and, particularly, ΔV, is the principal challenge of the approach.

C. Diagonalization of $\hat{H}_F$

1. Extraction of V_F from V

To obtain the 3D frame potential V_F from the full PES V, we have used two different procedures. In the first, we have simply fixed the six angle variables ω to values close to those characterizing the equilibrium trimer geometry. In particular, we have set each $\omega_k = (\theta_k,\phi_k)$ to $\bar{\omega} = (\bar{\theta},\bar{\phi}) = (90^\circ, 60^\circ)$ and have defined the corresponding V_F as

$$V_F^{(\bar{\omega})}(R_1,R_2,R_3;\bar{r}) \equiv \frac{V(R_1,R_2,R_3;\bar{\omega},\bar{r}) + V(R_2,R_1,R_3;\bar{\omega},\bar{r})}{2}. \quad (17)$$

The average on the rhs of Eq. (17) is necessary to make the function invariant to the operations of G_{12}.

In the second procedure, we have computed for each R point of interest a Gaussian-weighted-average of V over the six angle variables,

$$V_F^{(\mathrm{avg})}(R;\bar{r}) \equiv \sum_{i_1,i_2,i_3=-n_\theta}^{n_\theta}\sum_{j_1,j_2,j_3=-n_\phi}^{n_\phi} w_\theta(\theta_{i_1})w_\phi(\phi_{j_1}) \times w_\theta(\theta_{i_2})w_\phi(\phi_{j_2})w_\theta(\theta_{i_3})w_\phi(\phi_{j_3}) \times V(R,\theta_{i_1},\phi_{j_1},\theta_{i_2},\phi_{j_2},\theta_{i_3},\phi_{j_3};\bar{r}). \quad (18)$$

Here, the weight functions, w_θ and w_ϕ, are Gaussians chosen to approximate the angle probability distributions of the $\hat{H}_B$ ground state

$$w_\theta(\theta_i) = A_\theta \exp\left[-(\theta_i-\theta_0)^2/2\sigma_\theta^2\right] \quad (19)$$

and

$$w_\phi(\phi_j) = A_\phi \exp\left[-(\phi_j-\phi_0)^2/2\sigma_\phi^2\right], \quad (20)$$

where A_θ and A_ϕ are normalization constants, $\theta_0 = 90^\circ$, $\phi_0 = 57^\circ$, $\sigma_\theta = 13^\circ$, and $\sigma_\phi = 13^\circ$. Finally, the θ_i and ϕ_j were taken as

$$\theta_i = \theta_0 + \frac{i}{n_\theta}3\sigma_\theta \quad (i = -n_\theta,\ldots,n_\theta), \qquad \phi_j = \phi_0 + \frac{j}{n_\phi}3\sigma_\phi \quad (j = -n_\phi,\ldots,n_\phi), \quad (21)$$

with $n_\theta = n_\phi = 6$.

We have solved for the eigenvectors of $\hat{H}_F$ by taking V_F to be both $V_F^{(\bar{\omega})}$ and $V_F^{(\mathrm{avg})}$ and have constructed different 9D bases from these different solutions. Of course, for a given value of $\bar{r}$, these different 9D bases should produce the same results in a converged 9D calculation. One might expect, however, that a basis with a better overlap with the 9D eigenstates might be achievable by using the frame eigenstates corresponding to $V_F = V_F^{(\mathrm{avg})}$. We shall see below that this is, in fact, the case.

2. Basis and matrix elements

In order to diagonalize $\hat{H}_F$, we make use of a primitive basis consisting of 3D products of 1D potential-optimized discrete variable representation (PODVR)[57,58] functions

$$|n_1,n_2,n_3\rangle \equiv |R_{1,n_1}\rangle|R_{2,n_2}\rangle|R_{3,n_3}\rangle; \quad n_1,n_2,n_3 = 1,2,\ldots,N_R. \quad (22)$$

To compute the $|n_k\rangle$, we first solve the 1D eigenvalue equation corresponding to the operator

$$\hat{H}_{F,1}(R_1;\bar{R},\bar{\omega},\bar{r}) \equiv -\frac{1}{2\mu_1}\frac{\partial^2}{\partial R_1^2} + V_F^{(\bar{\omega})}(R_1;R_l = R_m = \bar{R},\bar{r}). \quad (23)$$

[Note that the 1D potential function in Eq. (23) is obtained from $V_F^{(\bar{\omega})}$ by evaluating the latter at fixed values of $R_2 = R_3 = \bar{R}$.] The eigenvalue equation is then solved by diagonalizing the $\hat{H}_{F,1}$ matrix expressed in a sinc-DVR basis consisting of 80 functions corresponding to quadrature points ranging from $R_1 = 4.0$ to 8.0 bohrs. We then diagonalize the matrix of R_1 in the basis consisting of the N_R lowest-energy eigenstates of $\hat{H}_{F,1}$ to obtain the $|R_{1,n_1}\rangle$. Since all

the R_k are symmetrically equivalent, the determination of the $|R_{1,n_1}\rangle$ produces the $|R_{2,n_2}\rangle$ and $|R_{3,n_3}\rangle$, as well.

The matrix elements of the $V' + V_F$ portion of $\hat{H}_F$ are diagonal and readily evaluated by quadrature in the basis of Eq. (22). To compute the $\hat{K}_F$ matrix elements in that basis, we make use of

$$\cos\alpha_k = \frac{R_l^2 + R_m^2 - R_k^2}{2R_lR_m} \tag{24}$$

to re-write the $\partial/\partial R_k$ terms in Eq. (5) as

$$\begin{aligned} -\frac{\cos\alpha_k}{2R_kR_lR_m}\left(\frac{R_l^2}{M_l}+\frac{R_m^2}{M_m}\right)\frac{\partial}{\partial R_k} \\ = \frac{1}{4}\left[\left(\frac{1}{M_lR_m^2}+\frac{1}{M_mR_l^2}\right)\left(R_k\frac{\partial}{\partial R_k}\right)\right. \\ \left. -\left(\frac{1}{\mu_k}+\frac{R_l^2}{M_lR_m^2}+\frac{R_m^2}{M_mR_l^2}\right)\left(\frac{1}{R_k}\frac{\partial}{\partial R_k}\right)\right], \end{aligned} \tag{25}$$

and the $\partial^2/(\partial R_l \partial R_m)$ terms as

$$\begin{aligned} -\frac{\cos\alpha_k}{M_k}\frac{\partial^2}{\partial R_l\partial R_m} = -\frac{1}{2M_k}\left[\left(R_l\frac{\partial}{\partial R_l}\right)\left(\frac{1}{R_m}\frac{\partial}{\partial R_m}\right)\right. \\ + \left(R_m\frac{\partial}{\partial R_m}\right)\left(\frac{1}{R_l}\frac{\partial}{\partial R_l}\right) \\ \left. - R_k^2\left(\frac{1}{R_l}\frac{\partial}{\partial R_l}\right)\left(\frac{1}{R_m}\frac{\partial}{\partial R_m}\right)\right]. \end{aligned} \tag{26}$$

From Eqs. (5), (25), and (26), one sees that the evaluation of five types of matrix elements in the 1D $|R_{i,n_i}\rangle$ PODVR basis is sufficient to obtain all the terms for the 3D $\hat{K}_F$ matrix elements: $\langle R_{i,n_i'}|(\partial^2/\partial R_i^2)|R_{i,n_i}\rangle$, $\langle R_{i,n_i'}|R_i(\partial/\partial R_i)|R_{i,n_i}\rangle$, $\langle R_{i,n_i'}|R_i^{-1}(\partial/\partial R_i)|R_{i,n_i}\rangle$, $\langle R_{i,n_i'}|R_i^2|R_{i,n_i}\rangle$, and $\langle R_{i,n_i'}|R_i^{-2}|R_{i,n_i}\rangle$. These matrix elements are readily obtained by transforming to the $|R_{i,n_i}\rangle$ basis the corresponding matrix elements evaluated numerically in the sinc-DVR basis that is used to diagonalize $\hat{H}_{F,k}$ (see above).

3. Symmetry considerations

$\hat{H}_F$ is invariant to the operations of the G_{12}[53] molecular symmetry group. Thus, each $|\rho\rangle$ obtained from the diagonalization of $\hat{H}_F$ transforms as one of the irreducible representations ("irrep") of that group. In fact, since all the R_i transform into themselves upon inversion, the $|\rho\rangle$ belong only to either the A_1', A_2', or E' irreps of G_{12} (the even-parity ones). Now, the categorization of a given computed $|\rho\rangle$ as either A_1' or A_2' is straightforwardly accomplished by numerical calculation of all the expectation values $\langle\rho|\hat{R}|\rho\rangle$, where $\hat{R}$ is an operation of G_{12}. These values, of course, are all real and of unit magnitude for states of A_1' and A_2' symmetry. For any given doubly degenerate (i.e., E') pair of orthogonal solutions $|\rho_{a'}\rangle$ and $|\rho_{b'}\rangle$, though, the two-by-two matrices composed of the elements $\langle\rho_i|\hat{R}|\rho_j\rangle$ $(i,j = a', b')$ are not, in general, fully specified *a priori*. However, one is free to choose orthogonal linear combinations of any such $|\rho_{a'}\rangle$, $|\rho_{b'}\rangle$ pair, linear combinations that we label $|\rho_a\rangle$ and $|\rho_b\rangle$, respectively, such that the latter do transform under G_{12} as a specific, predetermined E' representation. It is advantageous for our purposes to choose such an E' representation [that is, the matrices with elements $D_{i,j}^{(E')}(\hat{R}) \equiv \langle\rho_i|\hat{R}|\rho_j\rangle$, $i,j = a, b$] to be the one given in Sec. I of the supplementary material. To compute the $|\rho_i\rangle$ $(i = a, b)$ pair with the desired transformation properties from an arbitrary degenerate-pair solution to the $\hat{H}_F$ eigenvalue equation, $|\rho_i\rangle$ $(i = a', b')$, we use a two-step process. In the first step, we (i) diagonalize the two-by-two matrix consisting of the elements $\langle\rho_i|\hat{R}|\rho_j\rangle$ $(i,j = a', b')$ for $\hat{R} = (23)$, (ii) identify the resulting (23) eigenvector with eigenvalue equal to -1 as $|\rho_a\rangle$, and (iii) identify the other eigenvector, with (23) eigenvalue equal to $+1$, as $\delta|\rho_b\rangle$, where $\delta = \pm 1$ is to be determined. In the second, we evaluate the matrix element $\delta\langle\rho_b|(123)|\rho_a\rangle$. This matrix element equals $\pm\sqrt{3/4}$ for $\delta = \pm 1$. Hence, such evaluation yields the value of δ and thus the eigenvector $|\rho_b\rangle$. All of the doubly degenerate $|\rho_i\rangle$ that we report in Sec. III A and that we employ in the various 9D bases transform according to the specific E' representation given in the supplementary material.

D. Diagonalization of $\hat{H}_B$

1. Extraction of V_B from V

The bend potential function, V_B, depends on one's choices for the fixed intermonomer distances ($\bar{R}$) and the fixed intramonomer distances ($\bar{r}$). As to the latter, we have solved the bend eigenstate equation for the two values or $\bar{r}$: r_e and r_0. The different sets of bend eigenstates so obtained, when employed in 9D bases, may be expected to yield 9D results different from one another. We have also worked with different V_B obtained by using different values for $\bar{R}$ and the same value of $\bar{r}$. The $\bar{R}$ values used—4.90, 4.97, and 5.0 bohrs—are all in the vicinity of the typical expectation values $\langle R_k\rangle$ of about 4.99 bohrs, characterizing the lowest-energy frame eigenstates (see Table I). The different sets of bend eigenstates resulting from these different $\bar{R}$ values, when employed in 9D bases, should give rise to matching sets of 9D eigenstates, assuming that the 9D calculations are converged. We make use of this expectation to assess the degree of convergence of the 9D calculations.

2. Basis and symmetry considerations

In solving for the eigenvectors of $\hat{H}_B$, we employ a primitive basis of spherical-harmonic products, such as those used in Ref. 53,

$$|l_1m_1, l_2m_2, l_3m_3\rangle \equiv |l_1m_1\rangle|l_2m_2\rangle|l_3m_3\rangle, \tag{27}$$

where

$$|l_im_i\rangle \equiv Y_{l_i}^{m_i}(\theta_i, \phi_i), \tag{28}$$

$l_i = 0, 1, \ldots, l_{\max}$, and $m_i = -l_i, -l_i + 1, \ldots, l_i$ for $i = 1$–3.

We use the Chebyshev version[59] of filter diagonalization[60] in order to diagonalize the matrix of $\hat{H}_B$ in this basis. In this process, we exploit the G_{12} symmetry of $\hat{H}_B$ to solve separately for the eigenvalues and eigenvectors associated with eight symmetry blocks. Four of these blocks correspond to the A_1', A_2', A_1'', and A_2'' irreps of G_{12}, respectively. The other four correspond to the two sub-irreps of each of the 2D irreps E' and E''. We label these sub-irreps as E_a', E_b', E_a'', and E_b'', respectively. They correspond to the specific representations of the E' and E'' irreps given in the supplementary material. Functions that transform in the same way as the $|\rho_a\rangle$ states described in Sec. II C belong to sub-irrep E_a'. Ones that transform in the same way as the $|\rho_b\rangle$ belong to sub-irrep E_b'. Ones that have negative parity, but

TABLE I. Properties of the lowest-energy 3D eigenstates of $\hat{H}_F$ for $\bar{r} = r_e$ and $V_F = V_F^{(\mathrm{avg})}$. ΔE values are in cm^{-1}, while $\langle R_k \rangle$ and ΔR_k are in bohr.

	ΔE[a]	$\langle R_1 \rangle$ (ΔR_1)	$\langle R_2 \rangle$ (ΔR_2)	$\langle R_3 \rangle$ (ΔR_3)	Irrep	Assignment
1	0.00	4.987 (0.186)	4.987 (0.186)	4.987 (0.186)	A_1'	g.s.
2	161.56	4.999 (0.187)	5.035 (0.254)	5.035 (0.254)	E_a'	ν_{as}
3	161.56	5.046 (0.272)	5.011 (0.212)	5.011 (0.212)	E_b'	ν_{as}
4	184.09	5.034 (0.263)	5.034 (0.263)	5.034 (0.263)	A_1'	ν_{ss}
5	317.35	5.059 (0.278)	5.059 (0.278)	5.059 (0.278)	A_1'	$2\nu_{as}$
6	319.26	5.046 (0.253)	5.066 (0.290)	5.066 (0.290)	E_a'	$2\nu_{as}$
7	319.26	5.073 (0.301)	5.053 (0.266)	5.053 (0.266)	E_b'	$2\nu_{as}$
8	338.51	5.060 (0.285)	5.076 (0.313)	5.076 (0.313)	E_a'	$\nu_{as} + \nu_{ss}$
9	338.51	5.082 (0.321)	5.066 (0.295)	5.066 (0.295)	E_b'	$\nu_{as} + \nu_{ss}$
10	363.16	5.083 (0.324)	5.083 (0.324)	5.083 (0.324)	A_1'	$2\nu_{ss}$

[a]Energy relative to the ground-state energy of $-3785.16\ \mathrm{cm}^{-1}$.

otherwise transform like $|\rho_{(a/b)}\rangle$ with respect to the (123), (321), (12), (13), and (23) operations belong to sub-irreps E_a''/E_b''.

It is straightforward to show that the matrix of $\hat{H}_B$ is block-diagonal in the eight blocks corresponding to A_1', A_2', A_1'', A_2'', E_a', E_b', E_a'', and E_b''. Of course, the existence of blocks corresponding to the 1D irreps follows from group theory, as does that of blocks corresponding to the E' and E'' irreps. The existence of individual blocks corresponding to E_a' and E_b', and E_a'' and E_b'' can be proved by showing that matrix elements of the form $\langle a|\hat{H}_B|b\rangle$, where $|a\rangle$ transforms as E_a^s and $|b\rangle$ transforms as E_b^s ($s = '$ or $s = ''$) equal zero. We do so as follows:

$$\begin{aligned}\langle a|\hat{H}_B|b\rangle &= \langle a|(23)^{-1}(23)\hat{H}_B(23)^{-1}(23)|b\rangle \\ &= \langle a|(23)^{-1}\hat{H}_B(23)|b\rangle \\ &= \langle a|(-1)\hat{H}_B(+1)|b\rangle = -\langle a|\hat{H}_B|b\rangle = 0,\end{aligned} \tag{29}$$

where we have used $(23)\hat{H}_B(23)^{-1} = \hat{H}_B$, $(23)|a\rangle = -|a\rangle$, and $(23)|b\rangle = |b\rangle$.

To solve for the eigenstates of a given symmetry block via filter diagonalization, we start with a random state vector, $|\psi_0\rangle$, expressed in the primitive basis of Eq. (27) and project out of that vector the component that transforms according to the symmetry block. For any of the four 1D irreps, Γ, one has

$$|\psi_0^{(\Gamma)}\rangle = N\hat{P}^{(\Gamma)}|\psi_0\rangle, \tag{30}$$

where N is a normalization constant, and

$$\hat{P}^{(\Gamma)} \equiv \sum_{\hat{R}} [D^{(\Gamma)}(\hat{R})]^* \hat{R}. \tag{31}$$

$[D^{(\Gamma)}(\hat{R})$ is just the character corresponding to operation $\hat{R}$ for irrep Γ.] For any of the four sub-irreps, Γ_i,

$$|\psi_0^{(\Gamma_i)}\rangle = N\hat{P}_i^{(\Gamma)}|\psi_0\rangle; \qquad i = a, b, \tag{32}$$

where [e.g., see Eq. (49) of Ref. 53]

$$\hat{P}_i^{(\Gamma)} \equiv \sum_{\hat{R}} [D_{i,i}^{(\Gamma)}(\hat{R})]^* \hat{R}. \tag{33}$$

[Again, see Sec. I of the supplementary material for the diagonal matrix elements $D_{i,i}^{(E'/E'')}(\hat{R})$]. We then use $|\psi_0^{(\Gamma)}\rangle$ or $|\psi_0^{(\Gamma_i)}\rangle$ or as the initial state vector in the filter diagonalization procedure. Since $\hat{H}_B$ does not couple states belonging to different symmetry blocks, the eigenvectors ultimately produced by that procedure all have the same symmetry as the initial state vector. Of course, in order to make use of Eq. (30) or Eq. (32), one needs to know how the $\hat{R}$ of G_{12} transform the basis states defined in Eq. (27). This has been worked out by Wang and Carrington (see Table V of Ref. 53).

One advantage to choosing a specific representation for each of the E' and E'' irreps is that one need not directly compute both eigenstates of a degenerate pair by diagonalizing $\hat{H}_B$. If one computes one such state, say $|\kappa_a\rangle$, the other ($|\kappa_b\rangle$) follows from G_{12} symmetry transformation properties. For example, for both E' and E'' states,

$$(123)|\kappa_a\rangle = -\frac{1}{2}|\kappa_a\rangle + \sqrt{\frac{3}{4}}|\kappa_b\rangle. \tag{34}$$

Thus,

$$|\kappa_b\rangle = \frac{[(123) + 0.5]|\kappa_a\rangle}{\sqrt{3/4}}. \tag{35}$$

Therefore, with $|\kappa_a\rangle$ in hand from the diagonalization of $\hat{H}_B$, one can relatively trivially compute the corresponding $|\kappa_b\rangle$. We have made use of Eq. (35) in computing the bend eigenstates of E_b' and E_b'' symmetry. Hence, only six symmetry blocks of $\hat{H}_B$, rather than eight, were diagonalized in order to obtain the eigenstates of all symmetries.

3. Operation with $\hat{H}_B$

The Chebyshev filter-diagonalization[59] algorithm for the bend problem requires repeated operation of $\hat{H}_B$ [Eq. (12)] on state vectors expressed in the basis of Eq. (27). Such operation by the kinetic-energy portion of that operator is straightforwardly accomplished by direct matrix–vector multiplication, given that the relevant matrix elements in the primitive basis are easily evaluated analytically. Operation with the potential-energy term, $V_B(\omega; \bar{R}, \bar{r})$, on state vector $|\psi\rangle$ is accomplished by first transforming $|\psi\rangle$ from

the spherical-harmonic basis to a 6D Gauss quadrature grid composed of Gauss–Legendre quadrature points covering the θ_k degrees of freedom and Fourier quadrature points covering the ϕ_k degrees of freedom. The grid representation of $|\psi\rangle$ is then multiplied at each grid point by the value of V_B at that point. Finally, the result is transformed back to the $|l_1 m_1, l_2 m_2, l_3 m_3\rangle$ representation. The process is similar to that represented by Eqs. (45) and (46) of Ref. 53 except that, for the basis-to-grid step, the transformations to the polar-angle grid points here are all performed first, followed by a 3D fast Fourier transform to the azimuthal grid points. The inverse, grid-to-basis transformations follow in reverse order after multiplication by V_B.

For operation with V_B, we also experimented with a process involving transformation to and from a Lebedev grid, such as that employed in Ref. 61. We found that process to be slower than that involving the Gauss grid, despite the required Gauss grid being larger than the required Lebedev grid for a given primitive basis-set size. (The problem, as pointed out by Wang and Carrington,[56] stems from the non-direct-product nature of the Lebedev grid.) That said, use of a Lebedev grid to compute potential-energy matrix elements *is* advantageous in the diagonalization of the full 9D $\hat{H}$, as we describe in Sec. II E 4.

E. Diagonalization of the 9D Hamiltonian $\hat{H}$

1. Symmetry-adapted basis

In solving the 9D frame/stretch-bend problem, product functions composed of eigenfunctions of the 3D frame ($|\rho\rangle$) and 6D bend ($|\kappa\rangle$) eigenvalue equations, respectively, are used to construct the basis. Since it is desirable to block diagonalize the Hamiltonian, $\hat{H}$, into the eight blocks associated with the G_{12} irreps and sub-irreps as described earlier for the bend problem, we construct symmetry-adapted functions from such products and use the former in the 9D basis.

This symmetry-adaptation process is trivial when the symmetry of $|\rho\rangle$ (i.e., Γ_ρ) and/or that of $|\kappa\rangle$ (i.e., Γ_κ) corresponds to one of the proper 1D irreps. In those cases, the symmetry of $|\rho,\kappa\rangle \equiv |\rho\rangle|\kappa\rangle$ is well-defined and given by $\Gamma_{9D} = \Gamma_\rho \otimes \Gamma_\kappa$.

However, the situation is more complicated when $\Gamma_\rho = E'_{a/b}$ and $\Gamma_\kappa = E^s_{a/b}$ ($s = '$ or $s = ''$). This is because $E' \otimes E' = A'_1 + A'_2 + E'$ and $E' \otimes E'' = A''_1 + A''_2 + E''$. Therefore, one has to construct functions of well-defined symmetry from linear combinations of the four product states $|\rho_a,\kappa_a\rangle$, $|\rho_a,\kappa_b\rangle$, $|\rho_b,\kappa_a\rangle$, and $|\rho_b,\kappa_b\rangle$. This can be accomplished by making use of the projection operator given in Eq. (33). Ultimately, one obtains

$$|\rho,\kappa\rangle_{A^s_1} = \frac{|\rho_a,\kappa_a\rangle + |\rho_b,\kappa_b\rangle}{\sqrt{2}}, \tag{36}$$

$$|\rho,\kappa\rangle_{A^s_2} = \frac{|\rho_a,\kappa_b\rangle - |\rho_b,\kappa_a\rangle}{\sqrt{2}}, \tag{37}$$

$$|\rho,\kappa\rangle_{E^s_a} = \frac{|\rho_a,\kappa_b\rangle + |\rho_b,\kappa_a\rangle}{\sqrt{2}}, \tag{38}$$

$$|\rho,\kappa\rangle_{E^s_b} = \frac{|\rho_a,\kappa_a\rangle - |\rho_b,\kappa_b\rangle}{\sqrt{2}}, \tag{39}$$

where the subscript on the lhs of each of Eqs. (36)–(39) corresponds to Γ_{9D} for the basis state.

2. Matrix elements—General

There are three types of nontrivial matrix-element calculations that must be performed to compute the matrix of $\hat{H}$ in the 9D basis. These correspond to the operators $\hat{K}_{FM}$ [Eq. (7)], $\Delta\hat{K}_M$ [Eqs. (14), (3), and (4)], and ΔV [Eq. (15)]. For each of these operators, $\hat{O}$, we calculate the quantities $\langle\rho',\kappa'|\hat{O}|\rho,\kappa\rangle$ for all relevant product basis functions $|\rho',\kappa'\rangle$ and $|\rho,\kappa\rangle$. We then use those results to construct the matrix elements of $\hat{O}$ in the 9D symmetry-adapted basis. This is trivial when $|\rho'\rangle$, $|\kappa'\rangle$, $|\rho\rangle$, and $|\kappa\rangle$ all transform as 1D irreps of G_{12}. However, when both $|\rho'\rangle$ and $|\kappa'\rangle$ and/or $|\rho\rangle$ and $|\kappa\rangle$ are of E-type symmetry, it is necessary to go one step further and make use of Eqs. (36)–(39) in conjunction with the $\langle\rho',\kappa'|\hat{O}|\rho,\kappa\rangle$ values to obtain the symmetry-adapted matrix elements.

3. Kinetic-energy matrix elements

Since both $\hat{K}_{FM}$ and $\Delta\hat{K}_M$ are both operators of the form

$$\hat{O}(R,\omega) = \sum_i \hat{O}_{F,i}(R)\hat{O}_{B,i}(\omega), \tag{40}$$

each of the matrix elements of these operators in the $|\rho,\kappa\rangle$ basis is readily factored into a sum of products of terms, such as

$$\langle\rho',\kappa'|\hat{O}_{F,i}\hat{O}_{B,i}|\rho,\kappa\rangle = \langle\rho'|\hat{O}_{F,i}(R)|\rho\rangle\langle\kappa'|\hat{O}_{B,i}(\omega)|\kappa\rangle. \tag{41}$$

Thus, while the full matrix elements are nominally 9D integrals, the cost of their evaluation is effectively that of the 6D ω matrix elements in Eq. (41). The latter are straightforwardly computed since the $\hat{O}_{B,i}$ are monomer angular momentum operators of the form $\hat{I}_{k,z}$ ($k = 1$–3) or $\hat{I}_{k,\alpha}\hat{I}_{j,\beta}$ ($k,j = 1$–3 and $\alpha,\beta = x,y,z$) and the $|\kappa\rangle$ are expressed in the spherical-harmonic product basis [Eq. (27)].

Our evaluation of the $\langle\rho'|\hat{O}_{F,i}|\rho\rangle$ matrix elements makes use of

$$\langle\rho'|\hat{O}_{F,i}|\rho\rangle = \sum_{n',n}\langle\rho'|n'\rangle\langle n'|\hat{O}_{F,i}|n\rangle\langle n|\rho\rangle, \tag{42}$$

where $n' \equiv (n'_1, n'_2, n'_3)$ and $n \equiv (n_1, n_2, n_3)$. Computation of the $\langle n'|\hat{O}_{F,i}|n\rangle$ requires, in part, the evaluation of matrix elements in the 3D PODVR basis [Eq. (22)] of quantities, such as $\sin\alpha_k$, $\cos(\alpha_k/2)$, and $\sin(\alpha_k/2)$ [e.g., see Eqs. (8) and (9) and Eqs. (25) and (27) of Ref. 53], which are functions of all three frame coordinates that cannot be factored into terms involving single coordinates. We assume that such matrix elements are diagonal—that is, that they are accurately computed by quadrature over the 3D PODVR grid. In cases where portions of an operator $\hat{O}_{F,i}$ *can* be factored into terms depending on single coordinates, we evaluate matrix elements of those terms in the relevant 1D PODVR basis and employ the results in the evaluation of the full $\hat{O}_{F,i}$ matrix element.

As an example of the above, consider

$$\hat{O}_{F,i} \equiv \frac{S}{M_1}\frac{1}{R_2^2}\left(\frac{1}{R_3}\frac{\partial}{\partial R_3}\right), \tag{43}$$

where $S = \sin\alpha_1/(2R_2R_3)$. This is a term in the $\lambda_{1,z}$ operator of $\hat{K}_{FM}$ [see Eqs. (7) and (8)]. The matrix elements of this operator can be expressed as

$$\langle n|\hat{O}_{F,i}|n'\rangle \simeq \sum_{n'',n'''} \langle n|\frac{S}{M_1}|n''\rangle\langle n''|\frac{1}{R_2^2}|n'''\rangle\langle n'''|\left(\frac{1}{R_3}\frac{\partial}{\partial R_3}\right)|n'\rangle. \quad (44)$$

To evaluate this, we first take

$$\langle n|S|n''\rangle \simeq S(R_{1,n_1}, R_{2,n_2}, R_{3,n_3})\delta_{n,n''} \equiv S(n)\delta_{n,n''}, \quad (45)$$

from which it follows that

$$\langle n|\hat{O}_{F,i}|n'\rangle \simeq \delta_{n_1,n_1'}\frac{S(n)}{M_1}\langle n_2|\frac{1}{R_2^2}|n_2'\rangle\langle n_3|\left(\frac{1}{R_3}\frac{\partial}{\partial R_3}\right)|n_3'\rangle. \quad (46)$$

Evaluations of all the required $\langle n|\hat{O}_{F,i}|n'\rangle$ matrix elements were performed in analogous fashion.

4. ΔV matrix elements

To obtain the ΔV matrix elements, we first compute the quantities

$$\begin{aligned}\Delta V^{\kappa',\kappa}_{n_1,n_2,n_3} &\equiv \langle \kappa'; n_1, n_2, n_3|\Delta V(\omega, R_1, R_2, R_3)|\kappa; n_1, n_2, n_3\rangle \\ &= \langle \kappa'|\Delta V(\omega, R_{1,n_1}, R_{2,n_2}, R_{3,n_3})|\kappa\rangle \end{aligned} \quad (47)$$

for all n_1, n_2, n_3, and for all relevant κ', κ. Note that, for simplicity of notation, we have suppressed the parametric dependence of the ΔV function on the rhs of Eq. (47) on the $\bar{R}$, $\bar{\omega}$, and $\bar{r}$ values. [Use of Eq. (47) is very similar to the "F-matrix" approach introduced by Carrington *et al.*[62,63]] We evaluate the 6D integral on the rhs of Eq. (47) by quadrature over a (θ_k, ϕ_k), k = 1–3 Lebedev grid. To facilitate this, prior to any evaluation of Eq. (47), we transform all of the $|\kappa\rangle$ in the 9D basis to the Lebedev grid representation and store the results. Since any one $|\kappa\rangle$ appears in many different $\Delta V^{\kappa',\kappa}_{n_1,n_2,n_3}$, this saves considerable computation time and gives a significant advantage to the use of a Lebedev grid over that of the larger Gauss grid required to evaluate the integrals.[56]

With all the $\Delta V^{\kappa',\kappa}_{n_1,n_2,n_3}$ in hand, we then compute the desired matrix elements

$$\langle \rho', \kappa'|\Delta V|\rho, \kappa\rangle = \sum_{n_1,n_2,n_3} \langle \rho'|n_1, n_2, n_3\rangle\langle n_1, n_2, n_3|\rho\rangle \Delta V^{\kappa',\kappa}_{n_1,n_2,n_3} \quad (48)$$

for all relevant ρ', κ' and ρ, κ.

In the most expensive step of this two-step process—the multiple evaluations of Eq. (47) —exploitation of symmetry allows for a reduction in computational cost by more than an order of magnitude, and we take advantage of this. Specifically, we make use of

$$\begin{aligned}\Delta V^{\kappa',\kappa}_{n_1,n_2,n_3} &= \langle \kappa'; n_1, n_2, n_3|\hat{R}^{-1}[\hat{R}\Delta V(\omega, R_1, R_2, R_3)\hat{R}^{-1}]\hat{R}|\kappa; n_1, n_2, n_3\rangle \\ &= \langle \kappa'; n_1, n_2, n_3|\hat{R}^{-1}[\Delta V(\omega, R_1, R_2, R_3)]\hat{R}|\kappa; n_1, n_2, n_3\rangle \\ &= \Delta V^{\hat{R}\kappa',\hat{R}\kappa}_{\hat{R}(n_1,n_2,n_3)}, \end{aligned} \quad (49)$$

which follows when $\hat{R}$ is an operation of the G_{12} symmetry group. Now, if $|\kappa\rangle$ transforms like one of the four 1D irreps of G_{12},

$$\hat{R}|\kappa\rangle = D^{(\Gamma_\kappa)}(\hat{R})|\kappa\rangle. \quad (50)$$

If $|\kappa\rangle$ transforms according to one of the four 2D irreps, it is either of the type $|\kappa_a\rangle$ or $|\kappa_b\rangle$. In these cases, one then has

$$\hat{R}|\kappa_i\rangle = \sum_{j=a,b} D^{(\Gamma_\kappa)}_{ji}(\hat{R})|\kappa_j\rangle; \quad i = a, b. \quad (51)$$

Examine now Eq. (49) for several cases. Start with $\hat{R} = E^*$, in which case (i) all of the $\mathbf{D}^{(\Gamma)}(E^*)$ matrices are diagonal, (ii) all of these diagonal elements equal +1 for the A_1', A_2' and E' irreps, and all equal −1 for the A_1'', A_2'', and E'' irreps, respectively, and (iii) $E^*|n_1, n_2, n_3\rangle = |n_1, n_2, n_3\rangle$. Given all this, it is straightforward to show from Eq. (49) that

$$\Delta V^{\kappa',\kappa}_{n_1,n_2,n_3} = 0, \quad (52)$$

unless both $|\kappa'\rangle$ and $|\kappa\rangle$ are symmetric or both are antisymmetric with respect to inversion. Thus, there is no need to evaluate any $\Delta V^{\kappa',\kappa}_{n_1,n_2,n_3}$ when $|\kappa'\rangle$ and $|\kappa\rangle$ have opposite parity.

Second, consider the case when $|\kappa'\rangle$ and $|\kappa\rangle$ both transform as 1D irreps. Then, Eq. (49) can be written as

$$\Delta V^{\kappa',\kappa}_{n_1,n_2,n_3} = D^{(\Gamma_{\kappa'})}(\hat{R})D^{(\Gamma_\kappa)}(\hat{R})\Delta V^{\kappa',\kappa}_{\hat{R}(n_1,n_2,n_3)}. \quad (53)$$

One sees that knowledge of the transformation properties of $|\kappa'\rangle$ and $|\kappa\rangle$ with respect to $\hat{R}$ allows one to determine a matrix element at one 3D grid point, (n_1, n_2, n_3), given knowledge of a matrix element at a different grid point, $\hat{R}(n_1, n_2, n_3)$.

The third case is that in which $|\kappa'\rangle$ is doubly degenerate and $|\kappa\rangle$ is nondegenerate. Then, one has two relevant $|\kappa'\rangle$ states: $|\kappa_a'\rangle$ and $|\kappa_b'\rangle$ and thus two relevant versions of Eq. (49),

$$\Delta V^{\kappa_i',\kappa}_{n_1,n_2,n_3} = \sum_{j=a,b} D^{(\Gamma_{\kappa'})}_{ji}(\hat{R})D^{(\Gamma_\kappa)}(\hat{R})\Delta V^{\kappa_j',\kappa}_{\hat{R}(n_1,n_2,n_3)}; \quad i = a, b. \quad (54)$$

Hence, by evaluating $\Delta V^{\kappa_j',\kappa}_{\hat{R}(n_1,n_2,n_3)}$ for $j = a$ and b, one can also easily obtain $\Delta V^{\kappa_i',\kappa}_{n_1,n_2,n_3}$ for $i = a$, b. (Moreover, by using hermiticity, one also obtains $\Delta V^{\kappa,\kappa_j'}_{n_1,n_2,n_3}$ and $\Delta V^{\kappa,\kappa_j'}_{\hat{R}(n_1,n_2,n_3)}$ for $j = a$, b.) As an example, consider $\hat{R} = (123)$ with $\Gamma_{\kappa'} = E'$ and $\Gamma_\kappa = A_1'$. Then,

$$\begin{aligned} D^{(\Gamma_{\kappa'})}_{aa}(\hat{R}) &= D^{(\Gamma_{\kappa'})}_{bb}(\hat{R}) = -\frac{1}{2} \\ D^{(\Gamma_{\kappa'})}_{ab}(\hat{R}) &= -D^{(\Gamma_{\kappa'})}_{ba}(\hat{R}) = -\sqrt{\frac{3}{4}}, \end{aligned} \quad (55)$$

and $D^{(\Gamma_\kappa)}(\hat{R}) = 1$. Also, $\hat{R}(n_1, n_2, n_3) = (n_3, n_1, n_2)$. Accordingly, one has

$$\Delta V^{\kappa_a',\kappa}_{n_1,n_2,n_3} = -\frac{1}{2}\Delta V^{\kappa_a',\kappa}_{n_3,n_1,n_2} + \sqrt{\frac{3}{4}}\Delta V^{\kappa_b',\kappa}_{n_3,n_1,n_2} \quad (56)$$

and

$$\Delta V^{\kappa_b',\kappa}_{n_1,n_2,n_3} = -\sqrt{\frac{3}{4}}\Delta V^{\kappa_a',\kappa}_{n_3,n_1,n_2} - \frac{1}{2}\Delta V^{\kappa_b',\kappa}_{n_3,n_1,n_2}. \quad (57)$$

Finally, consider when both $|\kappa'\rangle$ and $|\kappa\rangle$ are both doubly degenerate (i.e., both are either of E' or of E'' symmetry, since they both

must transform the same way with respect to inversion). Then, one has four relevant bending states, $|\kappa_{a/b}\rangle$ and $|\kappa'_{a/b}\rangle$, and four relevant equations,

$$\Delta V^{\kappa'_i,\kappa_j}_{n_1,n_2,n_3} = \sum_{k=a,b}\sum_{l=a,b} D^{(\Gamma)}_{ki}(\hat{R}) D^{(\Gamma)}_{lj}(\hat{R}) \Delta V^{\kappa'_k,\kappa_l}_{\hat{R}(n_1,n_2,n_3)}; \quad i = a,b \text{ and } j = a,b, \tag{58}$$

where Γ is either E' or E''. Clearly, knowledge of the four $\Delta V^{\kappa'_k,\kappa_l}_{\hat{R}(n_1,n_2,n_3)}$ yields the four $\Delta V^{\kappa'_k,\kappa_l}_{n_1,n_2,n_3}$, as well.

It is straightforward to assess the increase in efficiency when one makes full use of Eqs. (52)–(54) and (58) to compute the $\Delta V^{\kappa'\kappa}_{n_1,n_2,n_3}$. There is about a factor-of-two increase obtained by using parity. Within each parity block, the number of unique n_1, n_2, n_3 combinations that must be computed when symmetry is exploited is given by $N_R(N_R+1)(N_R+2)/6$. This compares with $(N_R)^3$ such combinations that must be computed when symmetry is neglected. Thus, in total, there is an efficiency increase equal to about a factor of $12(N_R)^2/[(N_R+1)(N_R+2)]$. A further increase by about a factor of two is obtained by making use of hermiticity.

One last means by which we have exploited symmetry so as to increase the efficiency of the $\Delta V^{\kappa'\kappa}_{n_1,n_2,n_3}$ calculations involves the integral over ω on the rhs of Eq. (47). Recall that we compute that 6D integral by quadrature on a Lebedev grid. Now consider how $\langle\omega|\kappa'\rangle$, $\langle\omega|\kappa\rangle$ and $\Delta V(\omega, R_{1,n_1}, R_{2,n_2}, R_{3,n_3})$ transform with respect to inversion. It is straightforward to show that

$$E^*\langle\omega|\kappa'\rangle = \langle\tilde{\omega}|\kappa'\rangle = \epsilon\langle\omega|\kappa'\rangle, \tag{59}$$

where $\tilde{\omega} \equiv E^*\omega$ and $\epsilon = \pm 1$ for even/odd-parity $|\kappa'\rangle$. Similarly,

$$E^*\langle\omega|\kappa\rangle = \langle\tilde{\omega}|\kappa\rangle = \epsilon\langle\omega|\kappa\rangle, \tag{60}$$

where the value of ϵ is the same as that in Eq. (59) since $|\kappa'\rangle$ and $|\kappa\rangle$ must have the same parity if Eq. (47) is to be nonzero. Since ΔV is invariant with respect to E^*, one also has

$$\Delta V(\tilde{\omega}, R_{1,n_1}, R_{2,n_2}, R_{3,n_3}) = \Delta V(\omega, R_{1,n_1}, R_{2,n_2}, R_{3,n_3}). \tag{61}$$

The upshot of all this is that

$$\langle\kappa'|\tilde{\omega}\rangle\Delta V(\tilde{\omega}, R_{1,n_1}, R_{2,n_2}, R_{3,n_3})\langle\tilde{\omega}|\kappa\rangle = \langle\kappa'|\omega\rangle\Delta V(\omega, R_{1,n_1}, R_{2,n_2}, R_{3,n_3})\langle\omega|\kappa\rangle. \tag{62}$$

That is, the integrand on the rhs of Eq. (47) is unchanged in going from ω to $\tilde{\omega}$. This means that in evaluating Eq. (47) one can reduce the size of the Lebedev grid by about a factor of two by including in the grid just one from each pair of quadrature points $(\omega_n, \tilde{\omega}_n)$. On this "half-grid," then

$$\Delta V^{\kappa',\kappa}_{n_1,n_2,n_3} \simeq \sum_{n=1}^{N_{\text{half}}} w_n^{(L)} w_n^{(\text{hgrid})} \times \langle\kappa'|\omega_n\rangle\langle\omega_n|\kappa\rangle\Delta V(\omega_n, R_{1,n_1}, R_{2,n_2}, R_{3,n_3}), \tag{63}$$

where $w_n^{(L)}$ is the Lebedev weight for the quadrature point ω_n, $w_n^{(\text{hgrid})} = 2$ if $\omega_n \neq E^*\omega_n$ and $w_n^{(\text{hgrid})} = 1$ if $\omega_n = E^*\omega_n$, and N_{half} is the size of the half-grid.

III. RESULTS AND DISCUSSION

A. 3D stretching eigenstates of $\hat{H}_F$

We have used bases corresponding to several values of N_R (12, 14, and 16) to test the convergence of the lowest-energy solutions to the $\hat{H}_F$ eigenvalue equation. For these basis-set sizes, direct diagonalization of $\hat{H}_F$ is quite feasible and was the means employed to solve for the $|\rho\rangle$. We find generally that for the 80 lowest-energy $|\rho\rangle$ (i.e., $N_F = 80$), there is no significant difference in going from the basis with $N_R = 12$ to that with $N_R = 16$. For $N_F = 150$, the $N_R = 14$ and $N_R = 16$ sets of solutions are substantially the same.

Table I summarizes results for the ten lowest-energy $|\rho\rangle$ for the $V_F = V_F^{(\text{avg})}(R; r_e)$. (The particular results shown are for $N_R = 14$.) It should be noted that, owing to the vibrational averaging, the ground-state expectation value of the intermonomer distances, $\langle R_k\rangle (k = 1–3)$, 4.987 bohrs, is significantly larger than the corresponding equilibrium value of 4.7601 bohrs on the same PES.[53] The latter was used in the quantum 6D calculations of the bending levels of $(HF)_3$.[53]

One sees that the states are assignable in terms of the degree of excitation in the frame symmetric- and asymmetric-stretching modes (ν_{ss} and ν_{as}, respectively). The computed fundamental frequencies of these two modes are 184.09 and 161.56 cm^{-1}, respectively. All of these energies, of course, depend on the particular choice of V_F. Table II shows how the values change when the choice of V_F changes. In particular, one sees by comparison of columns 2 and 3 of Table II that the method of extracting V_F from V has a significant effect on the frame eigenenergies, even when $\bar{r}$ does not change. Comparison of columns 3 and 4 shows that switching from $\bar{r} = r_e$ to $\bar{r} = r_0$ also changes the eigenenergies significantly, even though the method of ω-averaging used to produce V_F does not change. In respect to 9D results, the former differences should not matter in a converged calculation—the bases constructed, respectively, from the eigenstates corresponding to $V_F^{(\tilde{\omega})}(R; r_e)$ and to $V_F^{(\text{avg})}(R; r_e)$ address the same physical system. However, this is not true when $\bar{r}$ changes, and one expects differences in frame excitation energies to persist in going from 3D to 9D when $\bar{r}$ goes from r_e to r_0.

Several different sets of frame eigenstates were ultimately included in the bases for various 9D calculations. These sets are

TABLE II. Comparison of the 3D eigenenergies (in cm^{-1}) of $\hat{H}_F$ for different V_F. All energies are relative to the relevant ground-state energy listed for state No. 1. The different V_F are distinguished by the chosen value of the intramonomer distance, $\bar{r} = r_e$ or r_0 (in bohr), and by the method of angle averaging: fixed angles $(\tilde{\omega})$ or gaussian-averaged (avg). See text.

	$V_F^{(\tilde{\omega})}(R; r_e)$	$V_F^{(\text{avg})}(R; r_e)$	$V_F^{(\text{avg})}(R; r_0)$	Assignment
1	−4778.68	−3785.16	−3651.47	g.s.
2/3	179.46	161.56	165.60	ν_{as}
4	204.00	184.09	187.58	ν_{ss}
5	352.59	317.35	325.27	$2\nu_{as}(A'_1)$
6/7	355.11	319.26	327.26	$2\nu_{as}(E')$
8/9	376.17	338.51	346.00	$\nu_{as} + \nu_{ss}$
10	402.94	363.16	370.12	$2\nu_{ss}$

distinguished by (a) the number of frame states included, (b) the way in which the ω were treated in computing V_F (either "$\bar{\omega}$" or "avg"), (c) the size of the frame primitive basis (either $N_R = 12$ or 14), and (d) the choice of $\bar{r}$ (either r_e or r_0). In regard to (a) one 9D basis includes the lowest 101 frame eigenstates, representing excitation energies up to about 1065 cm^{-1}. All other bases include the 150 lowest-energy frame states, representing excitation energies up to about 1215 cm^{-1}. Table 1 of the supplementary material summarizes the characteristics of all 150 frame states included in one of the 9D bases. (The frame states in question correspond to $V_F = V_F^{\text{avg}}$, $N_R = 12$, and $\bar{r} = r_e$.)

B. 6D bending eigenstates of $\hat{H}_B$

Prior to considering the computational results pertaining to the bend eigenstates, there are several features of such eigenstates and the bending level structure, in general, that it is useful to remark upon. First, one expects, in zeroth order, two in-plane bending modes and two out-of-plane bending modes. In both cases, these include a singly degenerate symmetric mode—ν_{isb} (irrep A_1') and ν_{osb} (irrep A_1''), for the in- and out-of-plane cases, respectively—and two doubly degenerate asymmetric modes—ν_{iab} (irrep E') and ν_{oab} (irrep E'') for the in- and out-of-plane cases, respectively.

Second, given the large barrier to the conversion between the two equivalent equilibrium geometries of the trimer (requiring the concerted breaking and re-forming of three HF–HF hydrogen bonds), as well as the 6D bend results already reported in Ref. 53 for the SO-3 + HF3BG PES, one expects the associated splittings of the tunneling doublets of the low-energy bending states to be very small (of order 10^{-4} cm^{-1} or less). As a result, each bend eigenstate of $A_1'(A_1'')$ symmetry should have an almost equal-energy tunneling-doublet counterpart of $A_2'(A_2'')$ symmetry. Similarly, each bend eigenstate of $E_a'(E_a'')$ symmetry should have an almost equal-energy tunneling-doublet counterpart also of $E_a'(E_a'')$ symmetry. (Of course, each state of $E_a'(E_a'')$ symmetry also has an *exactly* equal-energy counterpart of $E_b'(E_b'')$ symmetry.)

Finally, one way to facilitate the assignment of the bending states is to examine 1D reduced probability densities (RPD) of those states as a function of the following symmetry coordinates: (1) $Q_{isb} \equiv \sqrt{1/3}(\phi_1 + \phi_2 + \phi_3)$, (2) $Q_{iab,a} \equiv \sqrt{1/2}(\phi_3 - \phi_2)$, (3) $Q_{iab,b} \equiv \sqrt{1/6}(2\phi_1 - \phi_2 - \phi_3)$, (4) $Q_{osb} \equiv \sqrt{1/3}(\theta_1 + \theta_2 + \theta_3)$,

TABLE III. Properties[a] of the lowest-energy 6D eigenstates of $\hat{H}_B$ for $\bar{R} = 5.0$ bohrs and $\bar{r} = r_e$.

	ΔE (cm^{-1})	$\langle\lvert\phi_1\rvert\rangle(\Delta\lvert\phi_1\rvert)$	$\langle\lvert\phi_2\rvert\rangle(\Delta\lvert\phi_2\rvert)$	$\langle\lvert\phi_3\rvert\rangle(\Delta\lvert\phi_3\rvert)$	$(\Delta\theta_1, \Delta\theta_2, \Delta\theta_3)$	Assign.
			A_1', A_2'[b]			
1	0.00	57.0 (11.5)	57.0 (11.5)	57.0 (11.5)	(12.4,12.4,12.4)	g.s.
2	720.10	59.7 (16.4)	59.7 (16.4)	59.7 (16.4)	(14.1,14.1,14.1)	ν_{isb}
3	757.18	57.0 (12.8)	57.0 (12.8)	57.0 (12.8)	(19.5,19.5,19.5)	$2\nu_{oab}$
4	933.81	59.5 (17.8)	59.5 (17.8)	59.5 (17.8)	(13.1,13.1,13.1)	$2\nu_{iab}$
5	1118.37	58.7 (13.3)	58.7 (13.3)	58.7 (13.3)	(18.8,18.8,18.8)	$2\nu_{osb}$
			E_a'[c]			
1/2	455.58	58.2 (11.9)	58.5 (17.3)	58.5 (17.3)	(12.7,12.7,12.7)	ν_{iab}
3/4	766.35	56.7 (12.3)	57.2 (12.6)	57.2 (12.6)	(19.3,20.8,20.8)	$2\nu_{oab}$
5/6	884.98	60.0 (19.5)	59.9 (19.3)	59.9 (19.3)	(13.3,13.2,13.2)	$2\nu_{iab}$
7/8	928.43	57.7 (13.4)	58.1 (13.2)	58.1 (13.2)	(20.5,19.1,19.1)	$\nu_{oab} + \nu_{osb}$
9/10	1102.38	61.6 (16.7)	61.5 (23.0)	61.5 (23.0)	(14.2,13.9,13.9)	$\nu_{iab} + \nu_{isb}$
			A_1'', A_2''[b]			
1	567.57	57.8 (12.2)	57.8 (12.2)	57.8 (12.2)	(15.8,15.8,15.8)	ν_{osb}
2	824.24	58.4 (16.3)	58.4 (16.3)	58.4 (16.3)	(17.1,17.1,17.1)	$\nu_{oab} + \nu_{iab}$
3	854.32	58.4 (16.2)	58.4 (16.2)	58.4 (16.2)	(16.8,16.8,16.8)	$\nu_{oab} + \nu_{iab}$
4	1120.36	57.2 (13.5)	57.2 (13.5)	57.2 (13.5)	(23.7,23.7,23.7)	$3\nu_{oab}$
5	1134.12	57.0 (13.2)	57.0 (13.2)	57.0 (13.2)	(23.5,23.5,23.5)	$3\nu_{oab}$
			E_a''[c]			
1/2	390.35	57.0 (11.9)	57.0 (11.9)	57.0 (11.9)	(16.8,16.6,16.6)	ν_{oab}
3/4	829.41	58.5 (16.6)	58.5 (16.3)	58.5 (16.3)	(17.0,17.2,17.2)	$\nu_{oab} + \nu_{iab}$
5/6	994.85	59.5 (18.9)	59.6 (16.0)	59.6 (16.0)	(17.0,16.4,16.4)	$\nu_{iab} + \nu_{osb}$
7/8	1086.05	59.4 (16.3)	58.7 (16.0)	58.7 (16.0)	(24.8,18.6,18.6)	$3\nu_{oab}/\nu_{oab} + \nu_{isb}$

[a]Energies are relative to the ground-state energy of −3568.82 cm^{-1}. Angles are in degrees.
[b]Each A_1' (A_1'') state has an A_2' (A_2'') counterpart of almost the same energy, as the tunneling splitings are much less than 0.01 cm^{-1}.
[c]Each E_a' and each E_a'' level is effectively two-fold (accidently) degenerate due to small tunneling splittings. Each such level also has a counterpart E_b' or E_b'' doublet of the same energy.

(5) $Q_{oab,a} \equiv \sqrt{1/2}(\theta_3 - \theta_2)$, and (6) $Q_{oab,b} \equiv \sqrt{1/6}(2\theta_1 - \theta_2 - \theta_3)$. As the notation suggests, each of these coordinates is associated with one of the expected bending modes. Hence, functions of the form

$$\mathrm{RPD}_\kappa(Q) = \int d\omega[\langle\kappa|\omega\rangle\delta(\omega - Q)\langle\omega|\kappa\rangle] \tag{64}$$

for a given bending state, $|\kappa\rangle$, should show evidence of node(s) if $|\kappa\rangle$ involves excitation of the mode associated with symmetry coordinate Q. It is largely based on the examination of plots of $\mathrm{RPD}_\kappa(Q)$ vs Q, in conjunction with other geometrical properties of the bend eigenstates (expectation values and standard deviations of the bend angles) that the bend assignments presented below have been made.

Table III shows selected results for the lowest-energy eigenstates of $\hat{H}_B$ computed for $\bar{R} = 5.0$ bohrs and $\bar{r} = r_e$. The basis set used to obtain these results (and all other bend results reported below) corresponds to $l_{\max} = 13$ and thus to a total size equal to $(196)^3$ or 7 529 536 functions. The Gauss grid employed for this basis is composed of 14 Gauss–Legendre quadrature points and 28 Fourier quadrature points for each of the three monomers, amounting to a total 6D grid size of 60 238 288 points. With this basis set, we estimate convergence to a few tenths of cm^{-1} for bend states up to at least 1500 cm^{-1} above the $\hat{H}_B$ ground state.

Listed in Table III are the computed energies of the bend eigenstates as well as the expectation values of the $|\phi_k|$ (denoted as $\langle|\phi_k|\rangle$) and the standard deviations of the $|\phi_k|$ (denoted as $\Delta|\phi_k|$) and the θ_k (denoted as $\Delta\theta_k$). (The expectation values of the θ_k are equal to 90° for all states.) From Table III, one sees that all four bending modes can be definitively assigned: These are ν_{iab} at 720.10 cm^{-1}, ν_{iab} at 455.58 cm^{-1}, ν_{osb} at 567.57 cm^{-1}, and ν_{oab} at 390.35 cm^{-1}. RPD plots that confirm these assignments are shown in Fig. 2. These assignments are also consistent with the geometrical properties listed in Table III for these states. As indicated in Table III, we have also made assignments (by the same procedure) of various low-energy bend eigenstates to overtones and combination bands of these four modes. Two examples, corresponding to $2\nu_{oab}(A_1')$ and $(\nu_{oab} + \nu_{osb})(E_a')$, are shown in Fig. 3. For both states one expects nodal structure in 1D RPD plots vs two different symmetry coordinates. Figure 3 shows both plots for each of the states. In both Figs. 2 and 3, we also show in each plot 1D cuts of the PES along the symmetry coordinate relevant to the plot. The 1D cuts were computed by fixing all the R_i and all the symmetry coordinates, apart from the one corresponding to the plot, to their equilibrium values.

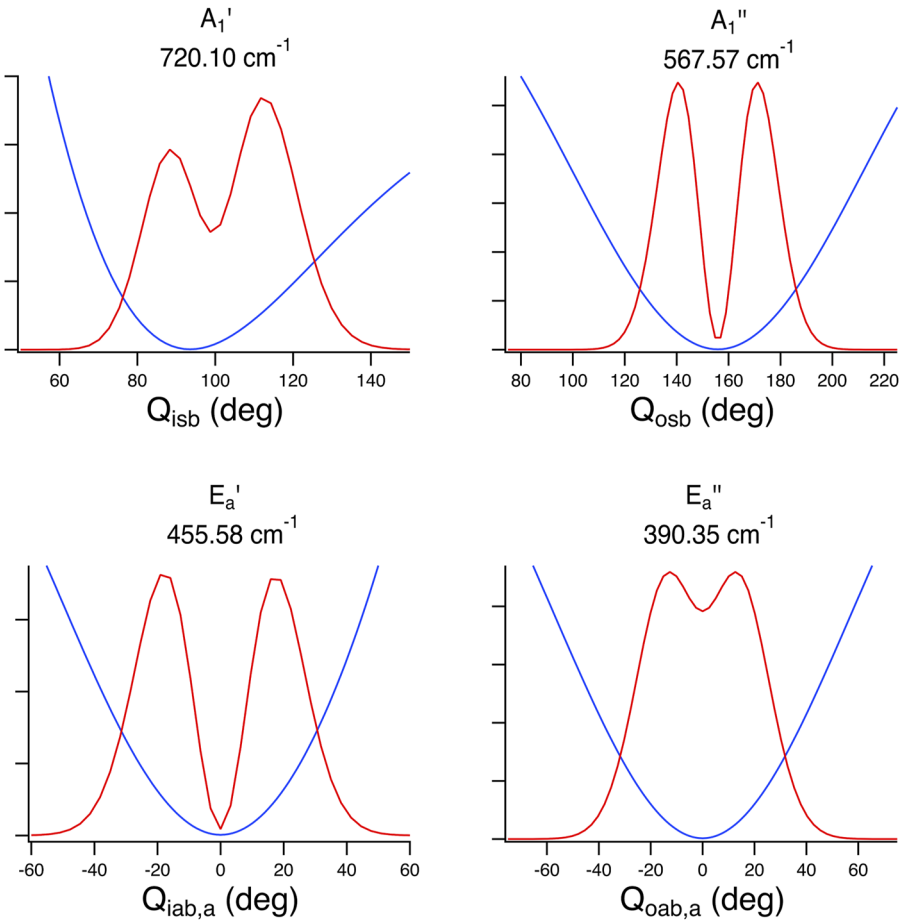

FIG. 2. 1D reduced probability densities (RPDs, red traces) as a function of symmetry coordinate (see Sec. III B for the symmetry-coordinate definitions) for four singly-excited bending eigenstates of HF trimer ($\bar{r} = r_e$ and $\bar{R} = 5.0$ bohrs). Top left: The ν_{isb} state. Top right: The ν_{osb} state. Bottom left: One of the $\nu_{iab}(E_a')$ states. Bottom right: One of the $\nu_{oab}(E_a'')$ states. Also plotted in each graph is the 1D SO-3 + HF3BG potential-energy cut (blue trace) along the relevant symmetry coordinate. Each PES cut corresponds to the five symmetry coordinates apart from the one varied in the plot and all three R_i being held constant at their equilibrium values. The RPDs and PES cuts have been scaled to fit on the same plot.

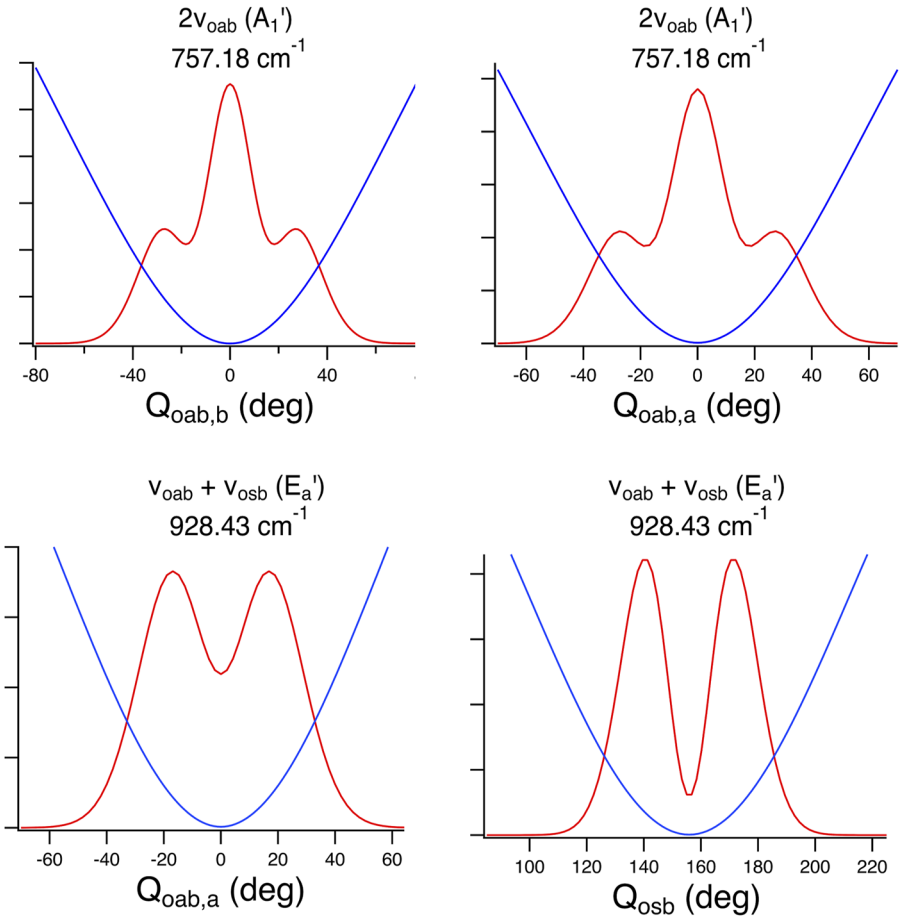

FIG. 3. 1D reduced probability densities (RPDs, red traces) as a function of symmetry coordinate for two doubly-excited bending eigenstates of HF trimer ($\bar{r} = r_e$ and $\bar{R} = 5.0$ bohrs). There are two plots for each state. Top: RPD of the $2\nu_{oab}(A_1')$ state plotted vs $Q_{oab,b}$ (left) and vs $Q_{oab,a}$ (right). Bottom: RPD of one of the $\nu_{oab} + \nu_{osb}$ states vs $Q_{oab,a}$ (left) and vs Q_{osb} (right). Also plotted in each graph is the 1D SO-3 + HF3BG potential-energy cut (blue trace) along the relevant symmetry coordinate. Each PES cut corresponds to the five symmetry coordinates apart from the one varied in the plot and all three R_i being held constant at their equilibrium values. The RPDs and PES cuts have been scaled to fit on the same plot.

Table IV presents results that illustrate how the eigenstates of $\hat{H}_B$ depend on the values of $\bar{R}$ and $\bar{r}$. One sees from the table that the bend level structure is significantly dependent on both of these parameters. One also notes two trends. First, increasing the intermonomer c.m.-to-c.m. distance $\bar{R}$ from 4.90 to 4.97 to 5.0 bohrs, all close to the ground-state expectation value of 4.99 bohrs (Table I), has the general effect of decreasing the frequencies of bend excitations. Second, increasing the intramonomer bond length from r_e to r_0 has the effect of increasing the frequencies of bend excitations. Both trends can be understood in terms of the effect of monomer–monomer "crowding" on the bending motions, as such crowding decreases with monomer–monomer distance and increases with monomer size.

The results of Table IV can be compared with the results obtained by Wang and Carrington[53,56] in their 6D calculations of the bend states of $(HF)_3$ on the SO-3 + HF3BG PES. Such comparison shows that our computed bend excitation frequencies are roughly 10% smaller than theirs. While, as pointed out earlier, our bend KEO is very slightly different than the properly constrained KEO of Wang and Carrington, such difference does not come close to accounting for the differences in bend eigenenergies. Instead, those differences are largely due to the considerably smaller (equilibrium) intermonomer distance assumed in Refs. 53 and 56—4.7601 bohrs—compared to the values that we have used, 4.90–5.0 bohrs. The marked effect of the choice of $\bar{R}$ (and $\bar{r}$) on the bend eigenstates obtained via 6D calculations is striking evidence of the significance of bend-stretch coupling in determining the nature of the vibrational states of the HF trimer, and the imperative to take it into account in accurate calculations.

In constructing various bases for solution of the 9D HF-trimer problem, we have included many more bending states than those listed in Tables III and IV. As one example, we include in the supplementary material (Table 2) a listing of the characteristics of all the bend states employed in one of the 9D bases we have used. The bend states in question correspond to $\bar{R} = 5.0$ bohrs and $\bar{r} = r_e$.

C. 9D intermolecular vibrational eigenstates of $\hat{H}$

We have diagonalized $\hat{H}$ by employing eight different 9D bases listed in Table V. Six of these bases (I to VI) pertain to $\bar{r} = r_e$ and the remaining two (VII and VIII) pertain to $\bar{r} = r_0$. The other relevant composition parameters for each of these bases are listed in Table V. The different compositions are distinguished not only by the numbers of frame and bend states included, but also by the treatment of the ω in determining V_F, the value of $\bar{R}$ in determining V_B, and the size of the primitive frame basis (as fixed by the value of N_R).

TABLE IV. Comparison of the lowest 6D eigenenergies (in cm^{-1}) of $\hat{H}_B$ for different V_B. Energies are relative to the relevant ground-state energy listed in the first line. The different V_B are distinguished by different values chosen for the fixed intermonomer distance [$\bar{R}$ (bohr)] and for the fixed intramonomer distance ($\tilde{r} = r_e$ or $\tilde{r} = r_0$), also in bohr. See text.

$(\bar{R}, \tilde{r})$ =	(4.9, r_e)	(4.97, r_e)	(5.0, r_e)	(4.97, r_0)	(5.0, r_0)	Assignment
			A_1', A_2'			
1	−3605.32	−3585.23	−3568.82	−3473.27	−3452.09	g.s.
2	765.39	733.40	720.10	743.07	729.47	ν_{isb}
3	798.69	769.46	757.18	780.01	767.38	$2\nu_{oab}$
4	995.43	951.73	933.81	963.80	945.41	$2\nu_{iab}$
5	1175.40	1135.24	1118.37	1147.87	1130.60	$2\nu_{osb}$
			E_a', E_b'			
1/2	489.12	465.35	455.58	472.26	462.25	ν_{iab}
3/4	808.28	778.76	766.35	789.82	777.04	$2\nu_{oab}$
5/6	950.20	904.04	884.98	917.85	898.34	$2\nu_{iab}$
7/8	978.62	943.21	928.43	955.18	939.99	$\nu_{oab} + \nu_{osb}$
9/10	1180.51	1125.17	1102.38	1142.56	1119.16	$\nu_{iab} + \nu_{isb}$
			A_1'', A_2''			
1	596.08	576.00	567.57	582.29	573.65	ν_{osb}
2	878.12	840.04	824.24	852.87	836.64	$\nu_{oab} + \nu_{iab}$
3	907.01	869.76	854.32	881.48	865.61	$\nu_{oab} + \nu_{iab}$
4	1183.67	1139.06	1120.36	1155.61	1136.34	$3\nu_{oab}$
5	1196.68	1152.62	1134.11	1169.10	1150.05	$3\nu_{oab}$
			E_a'', E_b''			
1/2	411.29	396.56	390.35	402.10	395.72	ν_{oab}
3/4	883.44	845.24	829.41	857.76	841.50	$\nu_{oab} + \nu_{iab}$
5/6	1057.32	1013.16	994.85	1026.79	1008.02	$\nu_{iab} + \nu_{osb}$
7/8	1150.81	1105.14	1086.05	1121.15	1101.52	$3\nu_{oab}$, $\nu_{oab} + \nu_{isb}$
9/10	1179.32	1135.17	1116.70	1150.18	1131.24	$3\nu_{oab}$, $\nu_{oab} + \nu_{isb}$

In all cases, the size of the primitive bend basis is the same, as fixed by $l_{max} = 13$. For each basis, the matrix of $\hat{H}$ expressed in each of the eight symmetry-adapted blocks of that basis is small enough to permit direct diagonalization of each block.

Table VI shows results pertaining to the computed eigenvectors of $\hat{H}$ for the six bases in Table V for which $\tilde{r} = r_e$. [The assignments presented in Table V have been made by examining the nature of the basis state(s) with the dominant contribution(s) to each 9D

TABLE V. Compositions[a] of the various 9D basis sets.

Basis	$\tilde{r}$	V_F type	N_R	N_F[b]	$\tilde{R}$ (bohr)[c]	N_B[d]	A_i states[e]	E_i states[f]
I	r_e	$\tilde{\omega}$	12	101	5.0	20	1360	2680
II	r_e	$\tilde{\omega}$	12	150	5.0	30	3030	5970
III	r_e	$\tilde{\omega}$	12	150	4.9	30	3030	5970
IV	r_e	Avg	12	150	5.0	30	3030	5970
V	r_e	Avg	12	150	4.97	30	3030	5970
VI	r_e	Avg	14	150	4.97	30	3030	5970
VII	r_0	Avg	12	150	5.0	30	3030	5970
VIII	r_0	Avg	12	150	4.97	30	3030	5970

[a]The V_F type and N_R values pertain to the computation of the frame states included in the 9D basis.
[b]N_F is the total number of frame states of all symmetries used to build the 9D basis.
[c]The $\tilde{R}$ values are those used to produce the bend states included in the 9D basis.
[d]N_B is the number of bend states belonging to each G_{12} irrep or sub-irrep used to build the 9D basis.
[e]"A_i states" refers to the number of states in the 9D basis having A_1', A_2', A_1'', or A_2'' symmetry.
[f]"E_i states" refers to the number of states in the 9D basis having E_a', E_b', E_a'', or E_b'' symmetry.

TABLE VI. Basis-set dependence of computed energies[a] for selected 9D eigenstates of $\hat{H}$ with $\bar{r} = r_e$. All energies are in cm^{-1}.

Basis	I	II	III	IV	V	VI	Assign.
				A_1', A_2'			
1	−3334.24	−3334.38	−3333.30	−3334.38	−3334.05	−3334.06	g.s.
2	181.96	181.78	181.52	181.80	181.73	181.72	ν_{ss}
3	311.17	311.09	311.38	311.09	311.23	311.23	$2\nu_{as}$
4	358.66	358.28	357.82	358.36	358.23	358.21	$2\nu_{ss}$
18	734.35	733.58	733.52	733.58	733.58	733.56	ν_{isb}
				E_a', E_b'			
1	161.08	161.07	160.83	161.06	161.04	161.07	ν_{as}
2	161.43	161.42	161.71	161.42	161.55	161.54	ν_{as}
3	314.70	314.59	314.12	314.60	314.54	314.57	$2\nu_{as}$
4	315.67	315.56	315.64	315.56	315.68	315.64	$2\nu_{as}$
9	466.59	466.36	466.92	466.37	466.58	466.57	ν_{iab}
10	467.77	467.54	468.30	467.55	467.54	467.47	ν_{iab}
				A_1'', A_2''			
1	528.20	527.95	530.53	527.95	528.86	528.85	$\nu_{as} + \nu_{oab}$
2	553.07	552.84	553.58	552.84	553.01	553.01	$\nu_{as} + \nu_{oab}$
3	586.51	586.21	584.70	586.21	585.68	585.67	ν_{osb}
				E_a'', E_b''			
1	393.99	393.91	393.97	393.91	393.99	394.00	ν_{oab}
2	394.36	394.28	395.09	394.28	394.41	394.40	ν_{oab}
3	544.63	544.36	544.40	544.35	544.41	544.44	$\nu_{as} + \nu_{oab}$
4	545.31	545.04	546.10	545.03	545.39	545.36	$\nu_{as} + \nu_{oab}$

[a]The listed energies (cm^{-1}) are all relative to the relevant ground-state energy except for the first listing in each column. The first listing in each column is the absolute energy of the ground-state.

eigenstate. More details on this are given below.] From these results, one can make several observations with respect to the degree of convergence of these low-energy 9D results. First, all of the bases give rise to absolute energies within about 1 cm^{-1} of each other and relative energies within several tenths of cm^{-1} of each other. Second, a comparison of the basis-I set of results with the basis-II set shows a small, though significant (several tenths of cm^{-1}) improvement in convergence obtained by increasing the numbers of frame and bend states (101–150 and 160–240 states, respectively). Third, the best sets of bend states employed in the 9D bases are those corresponding to $\bar{R}$ = 5.0 bohrs (i.e., bases I, II, and IV). Notably, $\bar{R}$ = 5.0 bohrs is the closest of the three values that we have employed to the $\langle R_k \rangle$ values characterizing the lowest-energy frame states (see Table I). Fourth, a test of the effect of N_R on 9D convergence, provided by comparing the results for bases V and VI, indicates very little effect due to the increase of that value from 12 to 14. This is an important result in that the 9D calculations for N_R = 12 can be accomplished roughly 1.59 times faster than those for N_R = 14. Finally, a comparison between the results for basis II and those for basis IV reveals very little difference on 9D convergence (at least for N_F = 150) due to using frame states computed with $V_F^{(\bar{\omega})}$ vs using ones computed with $V_F^{(\mathrm{avg})}$. This, despite the markedly different frame excitation energies, is associated with the two different approaches (see Table II).

Notwithstanding the final point made in the preceding paragraph, there is an advantage to employing in the 9D bases frame states obtained by using the $V_F^{(\mathrm{avg})}$ approach. In short, the use of such frame states produces more compact 9D bases than when the $V_F^{(\bar{\omega})}$-type states are used. This is evident from Table VII, when one examines the dominant basis-state norm (BSN) values for the computed 9D eigenstates given there. The BSN for 9D state $|I\rangle$ and dominant basis state $|\rho, \kappa\rangle$ is defined as BSN $\equiv |\langle \rho, \kappa | I \rangle|^2$. Table VII shows that the dominant BSNs of the selected low-energy 9D states are significantly larger for basis IV than for basis II. (Not coincidently, the 9D excitation energies are also much closer to the dominant basis-state excitation energies for basis IV than for basis II.) This certainly gives rise to a conceptual benefit in deciding on the nature of the 9D states. Moreover, one could presumably take advantage of the relative compactness of the $V_F^{(\mathrm{avg})}$ frame basis by working with smaller values of N_F to construct the 9D bases. Although we have not done that here, it could eventually prove valuable in extending the vibrational calculations on HF trimer to full dimensionality.

It is of interest to consider in more detail the results shown in Table VI obtained by using 9D bases in which everything is the same except for the value of $\bar{R}$ used to compute the bend eigenstates—for example, the results obtained with bases II and III and those obtained with bases IV and V (all from Table V).

TABLE VII. Properties of selected low-energy 9D eigenstates of $\hat{H}$ for $\bar{r} = r_e$, $\bar{R} = 5.0$ bohrs, and for the two different ways of obtaining V_F (i.e., two different sets of frame states). For each pair of numbers, x and y, listed as x/y, x pertains to $V_F^{(\mathrm{avg})}$ and y to $V_F^{(\bar{\omega})}$. The corresponding 9D bases are IV and II, respectively. All energies are in cm^{-1}.

	ΔE[a]	$\Delta E - \Delta E_{\mathrm{basis}}$[b]	BSN[c]	Assignment
		A_1', A_2'		
1	0.0/0.0	⋯	0.968/0.919	g.s.
2	181.80/181.78	−2.29/−23.22	0.913/0.760	ν_{ss}
3	311.09/311.09	−6.27/−41.50	0.919/0.824	$2\nu_{as}$
4	358.36/358.28	−4.80/−44.66	0.866/0.602	$2\nu_{ss}$
18	733.58/733.58	13.48/13.48	0.788/0.577	ν_{isb}
		E_a', E_b'		
1	161.06/161.07	−0.50/−18.39	0.955/0.885	ν_{as}
2	161.42/161.42	−0.24/−18.04	0.954/0.888	ν_{as}
9	466.37/466.36	10.79/10.78	0.766/0.625	ν_{iab}
10	467.55/467.54	11.97/11.96	0.760/0.621	ν_{iab}
		A_1'', A_2''		
1	527.95/527.95	−27.96/−41.86	0.801/0.652	$\nu_{as} + \nu_{oab}$
2	552.84/552.84	0.93/−16.97	0.958/0.783	$\nu_{as} + \nu_{oab}$
3	586.21/586.21	18.64/18.64	0.852/0.687	ν_{osb}
		E_a'', E_b''		
1	393.91/393.91	3.56/3.56	0.977/0.818	ν_{oab}
2	394.28/394.28	3.93/3.93	0.978/0.815	ν_{oab}
3	544.35/544.36	−7.56/−25.45	0.854/0.676	$\nu_{as} + \nu_{oab}$
4	545.03/545.04	−6.88/−24.78	0.865/0.691	$\nu_{as} + \nu_{oab}$

[a]Energy (cm^{-1}) relative to the ground-state energies −3334.38/−3334.38 cm^{-1}.
[b]$\Delta E_{\mathrm{basis}}$ is the excitation energy (cm^{-1}) of the dominant basis state.
[c]Basis-state norm. See text for definition.

Inspection of Table IV shows that the 6D bend level structures within each pair are qualitatively similar to one another but significantly different (by several percent) in a quantitative sense. Nevertheless, the 9D bend excitation energies in Table VI produced by each set in a given pair are well within a fraction of a percent of one another and also significantly different from the corresponding 6D bend energies. Clearly, there is bend/frame coupling that must be accounted for in order to obtain accurate bend (and for that matter, frame) excitation energies corresponding to a given trimer PES. The results from reduced dimension, constrained bend, or frame eigenvalue equations cannot be assumed to be quantitative reflections of the true intermolecular excitation energies.

Table VIII presents results for selected low-energy 9D states obtained for the two different values of $\bar{r}$ considered here. The relevant 9D bases for both $\bar{r} = r_e$ and $\bar{r} = r_0$ are basis IV and basis VII, respectively. These are equivalent in respect to the type of frame PES ($V_F^{(\mathrm{avg})}$) employed, the value of N_R, and that of $\bar{R}$. They also are both composed of the same number of frame states and the same number of bend states. Hence, the different results for the two bases can be confidently attributed to the two different $\bar{r}$ values. One sees from this table that changing from $\bar{r} = r_e$ to $\bar{r} = r_0$ results in the increase of all 9D excitation energies, those of the intermolecular fundamentals by 1%–3% and those of overtones and combination states by up to 4%. This implies that the excitation energies from the 9D rigid-monomer calculations of $(HF)_3$ have the uncertainty of several percent, depending on what $\bar{r}$ value is used.

Finally, Table IX compares the frequencies of selected intermolecular vibrational fundamentals of $(HF)_3$ from the 9D calculations in this work to those from the 6D bending-level calculations[53] and the relevant spectroscopic measurements in the gas phase[42] and in the neon matrix.[46] The 9D results are reported for two different values of $\bar{r}$, $\bar{r} = r_0$ and $\bar{r} = r_e$. The 6D results shown, from Ref. 53, were calculated using $\bar{r} = r_e$. The same SO-3 + HF3BG PES was used in both the 9D and the 6D calculations. The results in this table, theoretical and experimental, allow making several interesting comparisons that lead to a number of important insights. First, one can compare the results of the 9D and 6D calculations for $\bar{r} = r_e$. It is evident that they differ substantially for all bending fundamentals considered, those from our 9D calculation being about 10% smaller than their 6D counterparts. The only difference between the 9D and the 6D calculations is that the former rigorously include the intermolecular stretching vibrations and their coupling with the bending modes, while the 6D calculations do not. Consequently, the differences between the 9D and 6D results are due solely to the bend-stretch coupling that is present in the former but absent in the latter, thereby providing a direct measure of the importance of this coupling. Judging from the significant difference between the 9D and 6D results, the bend-stretch coupling is strong and cannot

TABLE VIII. Properties of selected low-energy 9D eigenstates of $\hat{H}$ for $\bar{r} = r_e$, basis set IV and $\bar{r} = r_0$, basis set VII. For each pair of numbers, x and y, listed as x/y, the first pertains to $\bar{r} = r_e$ and the second to $\bar{r} = r_0$. All energies are in cm^{-1}.

	ΔE[a]	Assignment	ΔE_{basis}[b]	BSN[c]
		A_1', A_2'		
1	0.0/0.0	g.s.	0.0/0.0	0.968/0.952
2	181.80/187.16	ν_{ss}	184.09/187.58	0.913/0.882
3	311.09/324.22	$2\nu_{as}$	317.36/325.27	0.919/0.916
4	358.36/368.99	$2\nu_{ss}$	363.16/370.12	0.866/0.823
18/17	733.58/755.59	ν_{isb}	720.10/729.47	0.788/0.708
		E_a', E_b'		
1	161.06/167.73	ν_{as}	161.56/165.60	0.955/0.946
2	161.42/167.96	ν_{as}	161.66/165.60	0.954/0.946
3	314.60/327.55	$2\nu_{as}$	319.26/327.26	0.866/0.856
4	315.56/328.45	$2\nu_{as}$	319.26/327.26	0.880/0.873
9	466.37/482.61	ν_{iab}	455.58/462.25	0.766/0.767
10	467.55/484.28	ν_{iab}	455.58/462.25	0.760/0.769
		A_1'', A_2''		
1	527.95/545.16	$\nu_{as} + \nu_{oab}$	551.91/561.32	0.801/0.777
2	552.84/570.66	$\nu_{as} + \nu_{oab}$	551.91/561.32	0.958/0.954
3	586.21/601.54	ν_{osb}	567.57/573.65	0.852/0.832
		E_a'', E_b''		
1	393.91/405.33	ν_{oab}	390.35/395.72	0.978/0.976
2	394.28/405.96	ν_{oab}	390.35/395.72	0.978/0.976
3	544.35/562.23	$\nu_{as} + \nu_{oab}$	551.91/561.32	0.853/0.858
4	545.03/562.66	$\nu_{as} + \nu_{oab}$	551.91/561.32	0.865/0.853

[a]Energy (cm^{-1}) relative to the ground-state energies −3334.38/−3452.09 cm^{-1}.
[b]Excitation energy (cm^{-1}) of the dominant basis state.
[c]Basis-state norm. See text for definition.

TABLE IX. Comparison of the frequencies (in cm^{-1}) of selected intermolecular vibrational fundamentals of $(HF)_3$ from the 9D calculations in this work with those from the 6D bending-level calculations and the spectroscopic measurements (Expt.). In the second column, for each pair of 9D values x and y, listed as x/y, the first pertains to $\bar{r} = r_0$ and the second to $\bar{r} = r_e$. The 6D results shown in the third column were calculated for $\bar{r} = r_e$. The same PES was used in both the 9D and the 6D calculations.

Assign.	9D (this work)	6D[a]	Expt.
ν_{as}	168/161	⋯	167 (Ne matrix)[b]
ν_{oab}	405/394	439	⋯
ν_{iab}	483/467	540	495 (gas phase)[c]
ν_{osb}	602/586	639	602 (gas phase)[c]
ν_{isb}	756/734	828	⋯

[a]Reference 53.
[b]Reference 46.
[c]Reference 42.

be neglected and has to be included in any quantitative treatment of the vibrations of $(HF)_3$. This also implies that the results of the 6D calculations that treat only the bend modes cannot be used to judge the accuracy of the PES employed. This is confirmed by the fact that the 9D results agree better with experimental gas-phase values available for two bending modes, ν_{iab} and ν_{osb}, than those from the 6D calculations. Evidently, the inclusion of the stretch-bend coupling improves the agreement between theory and experiment.

Despite the improvement over the 6D results (which are too high relative to experiment), the 9D results obtained for $\bar{r} = r_e$ are still visibly below the corresponding experimental values. However, Table IX also shows that using $\bar{r} = r_0$ in 9D calculations yields results in considerably better agreement with experimental data. Thus, the fundamental frequencies of the ν_{osb} and ν_{as} modes from the 9D calculations for $\bar{r} = r_0$ are in excellent agreement with the experimental values measured in the gas phase and Ne matrix, respectively. For the ν_{iab} mode, the agreement with experiment is only slightly worse, the calculated fundamental frequency being 12 cm^{-1}, or 2.5%, below measured gas-phase value.

It should not be surprising that the use of $\bar{r} = r_0$ (r_0 = 1.781 311 4 bohrs) in 9D calculations, instead of $\bar{r} = r_e$ (r_e = 1.763 794 8 bohrs), significantly improves the agreement between theory and the available experimental results. As stated in Sec. II A, r_e corresponds to the HF monomer equilibrium bond distance on the SO-3 + HF3BG surface. In contrast, r_0 is the ground-state expectation value of the HF monomer bond length from the reduced-dimension quantum 3D calculations of the intramolecular vibrational states of $(HF)_3$. In these calculations, the three intramolecular HF stretch coordinates are fully coupled, while the intermolecular coordinates of the trimer are frozen at $\bar{R}$ = 5.0 bohrs and $\bar{\omega} = (\bar{\theta}, \bar{\phi}) = (90°, 62°)$. This $\bar{R}$ is close to the ground-state expectation value of the intermonomer distance from the 3D calculations (Table I). Thus, $\bar{r} = r_0$ includes the effect of the vibrational averaging over the intramolecular ground-state wave function of $(HF)_3$, evidently non-negligible, while $\bar{r} = r_e$ does not.

It is clear from the above that definitive answers as to the accuracy of the SO-3 + HF3BG PES, or any other HF trimer PES that will become available in the future, will have to await the results of fully coupled quantum calculations encompassing all 12 dimensions.

One remaining important issue that we are uniquely positioned to address here is the importance of the three-body (HF3BG) term in the PES of the HF trimer. One way to assess its significance is to perform 9D quantum calculations of the intermolecular vibrational states of the trimer on the two-body (SO-3) PES, without the three-body term, and compare the results to those obtained already in 9D for the full SO-3 + HF3BG PES that includes both two- and three-body terms. Even a cursory comparison of this kind reveals large differences between these two sets of results. It suffices to consider just a few of the low-lying intermolecular stretching and bending states, in order to illustrate the major impact of the three-body term. In the following, for each intermolecular state listed a pair of energies (in cm^{-1}) is given as x/y, where x and y pertain to the energies calculated on the three-body and the 2+3-body PESs, respectively (the latter values are from Table VIII): ν_{as} = 118.02/161.06, ν_{ss} = 162.26/181.80, ν_{oab} = 307.56/393.91, ν_{iab} = 353.43/466.37, and ν_{osb} = 487.46/586.21. These energies are relative to the ground-state energies calculated for the two-body PES, −2786.4 cm^{-1}, and the 2+3-body PES, −3334.4 cm^{-1}, respectively; both are for $\bar{r} = r_e$. It is evident from this comparison that the vibrational energies computed on the two-body PES are all significantly lower than their counterparts obtained for the 2+3-body PES, and consequently in considerably worse agreement with the corresponding

experimental results in Table IX. From this, one can conclude that irrespective of the rather high quality of the SO-3 2-body potential, nonadditive three-body interactions play a large role and must be accounted for in order to construct an accurate PES of the hydrogen-bonded HF trimer. Good agreement with the pertinent spectroscopic results for $(HF)_3$ can be achieved only when the intermolecular vibrational eigenstates are calculated on a trimer PES that includes the three-body interactions. It is expected that this conclusion applies to other important hydrogen-bonded trimers, such as $(HCl)_3$ and $(H_2O)_3$.

IV. CONCLUSIONS

We have presented the computational methodology for efficient and rigorous 9D quantum calculations of the intermolecular vibrational states of noncovalently bound trimers of diatomic molecules. Its main target are the more strongly bound molecular trimers, such as the hydrogen-bonded HF and HCl trimers having many intermolecular vibrational states. The only dynamical approximation made in this treatment is keeping the bond lengths of the three monomers fixed. The rigid-monomer approximation is undoubtedly reasonable for such complexes, since the frequencies of the intramolecular stretching vibrations of the monomers are much higher than those of the intermolecular bending and stretching modes.

Our methodology employs the intermolecular trimer coordinates and the corresponding rigid-monomer 9D vibrational ($J = 0$) Hamiltonian of Wang and Carrington.[54] The nine intermolecular coordinates are comprised of the "frame" (or stretching) coordinates corresponding to the three monomer-c.m.-to-monomer-c.m. distances, and six "bend" coordinates describing the orientations of the monomers relative to the trimer triangular frame. A contracted-basis approach is used for calculating the fully coupled intermolecular eigenstates of the 9D Hamiltonian of the trimer. It is similar to that employed by Wang and Carrington in their 9D study of the vibrational states of methane.[56] It is also in the spirit of the approach that we have developed for calculating the rovibrational states of noncovalently bound molecular dimers in the product contracted basis of eigenstates of reduced-dimension Hamiltonians.[11,17] The full 9D trimer Hamiltonian, $\hat{H}$, is partitioned into a 3D "frame" Hamiltonian and a 6D "bend" Hamiltonian, $\hat{H}_F$ and $\hat{H}_B$, respectively. Each of the two Hamiltonians is diagonalized separately, and a certain number of their lowest-energy eigenstates with energies below the chosen cut-off values is included in the final 9D product contracted basis in which the full 9D intermolecular vibrational Hamiltonian is diagonalized. Of course, the cut-off values are varied, to assure that the results are converged.

This methodology is implemented in the 9D calculations of the intermolecular vibrational levels of $(HF)_3$, the first to fully include the coupling between the intermolecular bending and stretching vibrations of the trimer. These calculations employ the rigid-monomer version of the SO-3 + HF3BG surface computed by Quack, Stohner, and Suhm,[47] which includes one-, two-, and three-body terms. This PES depends on the choice of the fixed rigid-monomer bond distance, which we refer to as $\bar{r}$. In this work, results are obtained for two different values of $\bar{r}$. One of them, r_e, is the monomer equilibrium bond distance on the SO-3 + HF3BG surface.[53] The other, r_0, represents a very good estimate of the ground-state expectation value of the HF internuclear distance on that surface. The eigenstates of $\hat{H}_F$ are computed for the 3D frame potentials obtained by two procedures that differ in the way they deal with the bending angles, and for the two values of $\bar{r}$, r_e and r_0. The 6D eigenstates of $\hat{H}_B$ are calculated for several 6D bend potentials differing in the values of the fixed intermonomer distances, as well as for both $\bar{r}$ values. The objective of the preliminary calculations is to explore how these choices affect the convergence of the 9D eigenvalues of $\hat{H}$. The G_{12} symmetry of $(HF)_3$ is exploited to block-diagonalize the matrix of the full Hamiltonian $\hat{H}$ into the blocks associated with the G_{12} irreps, by constructing symmetry-adapted product-contracted basis functions and using them in the final 9D basis.

The results from the 9D calculations in this work are used to make two types of comparison. The first one is with the results of the 6D bending-level calculations,[53] for $\bar{r} = r_e$ and using the same SO-3 + HF3BG PES. For all bending fundamentals considered, their frequencies from our 9D calculations are about 10% lower than their 6D counterparts. These differences directly reflect the strength of the stretch-bend coupling, which is accounted for in the 9D calculations but is absent in the 6D calculations. The results make it clear that the stretch-bend coupling is strong and must be incorporated in any quantitative treatment of the $(HF)_3$ vibrations. The corollary is that 6D calculations that treat the bend modes of $(HF)_3$ only are not sufficient to assess the accuracy of the PES employed. This is supported by the observation that the 9D results agree better with the, admittedly limited, available spectroscopic data than those from the 6D calculations.

The second type of comparison is that of the 9D results obtained for $\bar{r} = r_e$ and $\bar{r} = r_0$, respectively, with the corresponding experimental values. One finds that the 9D calculations for $\bar{r} = r_0$ yield results that agree significantly better with experiment than those computed in 9D for $\bar{r} = r_e$. This is not surprising, given that $\bar{r} = r_0$ incorporates the effect of the vibrational averaging over the intramolecular ground-state wave function of $(HF)_3$ on the HF bond length, while $\bar{r} = r_e$ does not.

Our results show that, in general, replacing $\bar{r} = r_e$ with $\bar{r} = r_0$ in the 9D calculations leads to the increase of all excitation energies, the intermolecular fundamentals by 1%–3% and overtones and combination states by up to 4%. The implication is that the 9D rigid-monomer treatment of $(HF)_3$ introduces uncertainty of several percent in calculated excitation energies, depending on the $\bar{r}$ value employed. This residual uncertainty can be eliminated only by performing fully coupled quantum calculations of the vibrational levels of $(HF)_3$ in full dimensionality, including all 12 inter- and intramolecular degrees of freedom. Such extremely demanding calculations are under way in our group.

Finally, in order to get insight into the importance of the three-body interactions in the HF trimer, additional 9D quantum bound-state calculations are performed on the two-body (SO-3) trimer PES, in which the three-body term is not included. Intermolecular vibrational energies from these calculations are invariably significantly below those obtained for the 2+3-body SO-3 + HF3BG PES, and thus in worse agreement with experimental data. This leads to the conclusion that three-body interactions make a large contribution to the $(HF)_3$ PES, and must be included if accurate intermolecular vibrational eigenstates of the trimer are desired. It is to be

expected that the same conclusion is valid for other prototypical hydrogen-bonded trimers, e.g., $(HCl)_3$ and $(H_2O)_3$.

The methodology introduced here can be applied to other similar trimers, e.g., the HCl trimer. It also gives hope that in a not-too-distant future it may be possible to treat the H_2O trimer with the same level of rigor, at least in the rigid-monomer approximation.

SUPPLEMENTARY MATERIAL

The choice of representation for the doubly degenerate irreducible representation of G_{12} is given in Sec. 1 of the supplementary material. Table 1 of the supplementary material summarizes the characteristics of all 150 frame states included in one of the 9D bases. Table 2 of the supplementary material lists the characteristics of all the bend states employed in one of the 9D bases we have used.

ACKNOWLEDGMENTS

Z.B. and P.M.F. are grateful to the National Science Foundation for its partial support of this research through the Grant Nos. CHE-2054616 and CHE-2054604, respectively. P.M.F. is grateful to Professor Daniel Neuhauser for his support.

AUTHOR DECLARATIONS

Conflict of Interest

The authors have no conflicts to disclose.

Author Contributions

Peter M. Felker: Conceptualization (equal); Formal analysis (equal); Funding acquisition (equal); Methodology (equal); Writing – original draft (equal); Writing – review & editing (equal). **Zlatko Bačić**: Conceptualization (equal); Formal analysis (equal); Funding acquisition (equal); Methodology (equal); Writing – original draft (equal); Writing – review & editing (equal).

DATA AVAILABILITY

The data that support the findings of this study are available within the article and its supplementary material.

REFERENCES

[1] Z. Bačić and R. E. Miller, J. Phys. Chem. **100**, 12945 (1996).
[2] P. E. S. Wormer and A. van der Avoird, Chem. Rev. **100**, 4109 (2000).
[3] T. Carrington, Jr. and X.-G. Wang, Wiley Interdiscip. Rev.: Comput. Mol. Sci. **1**, 952 (2011).
[4] A. van der Avoird, "Vibration-rotation-tunneling levels and spectra of van der Waals molecules," in *Vibrational Dynamics of Molecules*, edited by J. M. Bowman (World Scientific, Singapore, 2022), p. 194.
[5] D. H. Zhang, Q. Wu, J. Z. H. Zhang, M. von Dirke, and Z. Bačić, J. Chem. Phys. **102**, 2315 (1995).
[6] Y. Qiu and Z. Bačić, J. Chem. Phys. **106**, 2158 (1997).
[7] Z. Bačić and Y. Qiu, "Vibration-rotation-tunneling dynamics of $(HF)_2$ and $(HCl)_2$ from full-dimensional quantum bound-state calculations," in *Advances in Molecular Vibrations and Collision Dynamics*, edited by J. M. Bowman and Z. Bačić (JAI Press, Inc., Stamford, 1998), Vol. 3, p. 183.
[8] Q. Wu, D. H. Zhang, and J. Z. H. Zhang, J. Chem. Phys. **103**, 2548 (1995).
[9] G. W. M. Vissers, G. C. Groenenboom, and A. van der Avoird, J. Chem. Phys. **119**, 277 (2003).
[10] J. Huang, D. Yang, Y. Zhou, and D. Xie, J. Chem. Phys. **150**, 154302 (2019).
[11] P. M. Felker and Z. Bačić, J. Chem. Phys. **151**, 024305 (2019).
[12] Y. Qiu, J. Z. H. Zhang, and Z. Bačić, J. Chem. Phys. **108**, 4804 (1998).
[13] C. Leforestier, F. Gatti, R. S. Fellers, and R. J. Saykally, J. Chem. Phys. **117**, 8710 (2002).
[14] C. Leforestier, K. Szalewicz, and A. van der Avoird, J. Chem. Phys. **137**, 014305 (2012).
[15] R. Schwan, C. Qu, D. Mani, N. Pal, L. van der Meer, B. Redlich, C. Leforestier, J. M. Bowman, G. Schwaab, and M. Havenith, Angew. Chem., Int. Ed. **58**, 13119 (2019).
[16] X.-G. Wang and T. Carrington, J. Chem. Phys. **148**, 074108 (2018).
[17] P. M. Felker and Z. Bačić, J. Chem. Phys. **153**, 074107 (2020).
[18] P. M. Felker and Z. Bačić, J. Phys. Chem. A **125**, 980 (2021).
[19] Y. Liu, J. Li, P. M. Felker, and Z. Bačić, Phys. Chem. Chem. Phys. **23**, 7101 (2021).
[20] P. M. Felker, Y. Liu, J. Li, and Z. Bačić, J. Phys. Chem. A **125**, 6437 (2021).
[21] P. M. Felker and Z. Bačić, Chin. J. Chem. Phys. **34**, 728 (2021).
[22] J. S. Mancini and J. M. Bowman, J. Phys. Chem. A **118**, 7367 (2014).
[23] D. Sabo, Z. Bačić, T. Bürgi, and S. Leutwyler, Chem. Phys. Lett. **244**, 283 (1995).
[24] D. Sabo, Z. Bačić, S. Graf, and S. Leutwyler, Chem. Phys. Lett. **261**, 318 (1996).
[25] D. Sabo, Z. Bačić, S. Graf, and S. Leutwyler, J. Chem. Phys. **110**, 5745 (1999).
[26] D. Sabo, Z. Bačić, S. Graf, and S. Leutwyler, J. Chem. Phys. **111**, 5331 (1999).
[27] D. Sabo, Z. Bačić, S. Graf, and S. Leutwyler, J. Chem. Phys. **111**, 10727 (1999).
[28] A. van der Avoird, E. H. T. Olthof, and P. E. S. Wormer, J. Chem. Phys. **105**, 8034 (1996).
[29] E. H. T. Olthof, A. van der Avoird, P. E. S. Wormer, K. Liu, and R. J. Saykally, J. Chem. Phys. **105**, 8051 (1996).
[30] M. Geleijns and A. van der Avoird, J. Chem. Phys. **110**, 823 (1999).
[31] T. Salmi, E. Sälli, and L. Halonen, J. Phys. Chem. A **116**, 5368 (2012).
[32] J. O. Jung and R. B. Gerber, J. Chem. Phys. **105**, 10332 (1996).
[33] R. Schwan, C. Qu, D. Mani, N. Pal, G. Schwaab, J. M. Bowman, G. S. Tschumper, and M. Havenith, Angew. Chem., Int. Ed. **59**, 11399 (2020).
[34] J. K. Gregory and D. C. Clary, J. Chem. Phys. **102**, 7817 (1995).
[35] J. O. Richardson, S. C. Althorpe, and D. J. Wales, J. Chem. Phys. **135**, 124109 (2011).
[36] C. L. Vaillant, D. J. Wales, and S. C. Althorpe, J. Phys. Chem. Lett. **10**, 7300 (2019).
[37] M. Eraković, C. L. Vaillant, and M. T. Cvitaš, J. Chem. Phys. **152**, 084111 (2020).
[38] L. S. Costa and D. C. Clary, J. Chem. Phys. **117**, 7512 (2002).
[39] H.-G. Yu, J. Chem. Phys. **120**, 2270 (2004).
[40] M. Quack and M. A. Suhm, "Spectroscopy and quantum dynamics of hydrogen fluoride clusters," in *Advances in Molecular Vibrations and Collision Dynamics*, edited by J. M. Bowman and Z. Bačić (JAI Press, Inc., Stamford, 1998), Vol. 3, p. 205.
[41] M. A. Suhm, J. T. Farrell, S. H. Ashworth, and D. J. Nesbitt, J. Chem. Phys. **98**, 5985 (1993).
[42] P. Asselin, P. Soulard, B. Madebène, M. Goubet, T. R. Huet, R. Georges, O. Pirali, and P. Roy, Phys. Chem. Chem. Phys. **16**, 4797 (2014).
[43] D. W. Michael and J. M. Lisy, J. Chem. Phys. **85**, 2528 (1986).
[44] K. D. Kolebrander, C. E. Dykstra, and J. M. Lisy, J. Chem. Phys. **88**, 5995 (1988).
[45] L. Andrews, V. E. Bondybey, and J. H. English, J. Chem. Phys. **81**, 3452 (1984).
[46] L. Andrews, S. R. Davis, and R. D. Hunt, Mol. Phys. **77**, 993 (1992).
[47] M. Quack, J. Stohner, and M. A. Suhm, J. Mol. Struct. **294**, 33 (1993).
[48] M. Quack, J. Stohner, and M. A. Suhm, J. Mol. Struct. **599**, 381 (2001).
[49] M. Quack and M. A. Suhm, J. Chem. Phys. **95**, 28 (1991).
[50] W. Klopper, M. Quack, and M. A. Suhm, J. Chem. Phys. **108**, 10096 (1998).
[51] A. Io, T. Kawatsu, and M. Tachikawa, J. Phys. Chem. A **123**, 7950 (2019).
[52] G. M. Chaban and R. B. Gerber, Spectrochim. Acta, Part A **58**, 887 (2002).
[53] X.-G. Wang and T. Carrington, Jr., J. Chem. Phys. **115**, 9781 (2001).
[54] X.-G. Wang and T. Carrington, Jr., Can. J. Phys. **79**, 623 (2001).

[55]E. B. Wilson, J. C. Decius, and P. C. Cross, *Molecular Vibrations: The Theory of Infrared and Raman Vibrational Spectra* (McGraw-Hill, New York, 1955).
[56]X.-G. Wang and T. Carrington, Jr., J. Chem. Phys. **119**, 101 (2003).
[57]H. Wei and T. Carrington, Jr., J. Chem. Phys. **97**, 3029 (1992).
[58]J. Echave and D. C. Clary, Chem. Phys. Lett. **190**, 225 (1992).
[59]V. A. Mandelshtam and H. S. Taylor, J. Chem. Phys. **106**, 5085 (1997).
[60]M. R. Wall and D. Neuhauser, J. Chem. Phys. **102**, 8011 (1995).
[61]X.-G. Wang and T. Carrington, Jr., J. Theor. Comput. Chem. **2**, 599 (2003).
[62]M. J. Bramley and T. Carrington, Jr., J. Chem. Phys. **101**, 8494 (1994).
[63]X.-G. Wang and T. Carrington, Jr., J. Chem. Phys. **117**, 6923 (2002).